

Predicting the Heaviest Black Holes below the Pair Instability Gap

Ethan R. J. Winch,^{1,2*} Jorick S. Vink,¹ Erin R. Higgins¹ and Gautham N. Sabhahit^{1,2}

¹*Armagh Observatory and Planetarium (AOP), Armagh, College Hill, BT61 9DB*

²*School of Maths and Physics, Queen's University Belfast, Northern Ireland, University Road, BT7 1NN*

Accepted 2024 January 25. Received 2024 January 24; in original form 2023 June 14

ABSTRACT

Traditionally, the pair instability (PI) mass gap is located between 50 and 130 M_{\odot} , with stellar mass black holes (BHs) expected to "pile up" towards the lower PI edge. However, this lower PI boundary is based on the assumption that the star has already lost its hydrogen (H) envelope. With the announcement of an "impossibly" heavy BH of 85 M_{\odot} as part of GW 190521 located inside the traditional PI gap, we realised that blue supergiant (BSG) progenitors with small cores but large Hydrogen envelopes at low metallicity (Z) could directly collapse to heavier BHs than had hitherto been assumed. The question of whether a single star can produce such a heavy BH is important, independent of gravitational wave events. Here, we systematically investigate the masses of stars inside the traditional PI gap by way of a grid of 336 detailed MESA stellar evolution models calculated across a wide parameter space, varying stellar mass, overshooting, rotation, semi-convection, and Z . We evolve low Z stars in the range $10^{-3} < Z/Z_{\odot} < Z_{\text{SMC}}$, making no prior assumption regarding the mass of an envelope, but instead employing a wind mass loss recipe to calculate it. We compute critical Carbon-Oxygen and Helium core masses to determine our lower limit to PI physics, and we provide two equations for M_{core} and M_{final} that can also be of use for binary population synthesis. Assuming the H envelope falls into the BH, we confirm the maximum BH mass below PI is $M_{\text{BH}} \approx 93.3 M_{\odot}$. Our grid allows us to populate the traditional PI gap, and we conclude that the distribution of BHs above the traditional boundary is not solely due to the shape of the initial mass function (IMF), but also to the same stellar interior physics (i.e. mixing) that which sets the BH maximum.

Key words: stars: massive – stars: black holes – stars: evolution – stars: supergiants – stars: Population II

1 INTRODUCTION

The outcomes from stellar evolution of the most massive stars are still highly uncertain, but could involve pair instability supernovae (PISNe) or black hole (BH) formation above and below the Pair Instability (PI) range. An accurate mapping of these outcomes is critical for our understanding of chemical evolution, as a full-fledged PI completely disrupts the entire star, enriching the environment, while a direct collapse to a BH implies no chemical enrichment at all (Woosley et al. 2002; Langer 2012; Yusof et al. 2013; Limongi & Chieffi 2018; Higgins et al. 2021; Volpato et al. 2023). The key factors deciding these outcomes involve the stellar core and envelope masses, with the former mostly set by the initial mass (M_{ZAMS}) and amount of overshooting, and the latter by metallicity-dependent stellar winds (Vink et al. 2021; Tanikawa et al. 2021; Costa et al. 2022). While direct observations of PISNe have been controversial (Gal-Yam et al. 2009; Schulze et al. 2023), a new window that could help address this question has opened up through the discovery of gravitational waves (GWs) from BH mergers by LIGO/VIRGO (Abbott et al. 2016). While for a full analysis of BH masses from LIGO/VIRGO one would need to employ binary evolution and/or cluster dynamical simulations, specific features in the GW distribution, such as the maximum BH mass, are fundamental for all of massive star evolution, and not just for the small fraction of stars that eventually take part in a GW event.

Prior to the first GW event, most BH masses in our Milky Way had been determined from electromagnetic information yielding values up to just 10–20 M_{\odot} (e.g. Orosz et al. 2011; Casares & Jonker 2014). However the first GW event 150914 had components in the 30–40 M_{\odot} range, which could most easily be explained by a reduced Z content in a lower Z galaxy (e.g. Belczynski et al. 2010; Spera et al. 2015) where wind mass loss from massive Wolf-Rayet (WR) stars driven by iron (Fe) ions would be expected to be lower (Vink & de Koter 2005). Subsequent BH merger events also appear to "pile up" towards the $\sim 35 M_{\odot}$ mark (Fishbach & Holz 2020; Kimball et al. 2021; Wang et al. 2022; Abbott et al. 2023), which may be caused by the lower edge of PI, which for stars that have lost their hydrogen (H) envelope is thought to be located at $\sim 50 M_{\odot}$ (Woosley 2017; Farmer et al. 2019; Renzo et al. 2020a). Note that pulsational PI (or PPI) may lower the maximum BH mass due to mass loss associated with pulses. So there are basically 2 lower edges to PI in the literature: one located in between direct BH formation versus the onset of PI physics, and a second one between PPI versus fully-fledged PISNe at higher masses. In this paper we focus on the former, with a boundary between direct BH collapse and the onset of PI physics, which turns out to be set by a critical core masses (for He and CO) that we consistently derive for objects with a large H envelope in this study.

A huge surprise came with the detection of BH masses above the traditional 50 M_{\odot} stellar BH limit. In particular GW 190521 (Abbott et al. 2020) showed the existence of two heavy BHs of 66^{+17}_{-18} and 85^{+21}_{-14} M_{\odot} merging into a product of 142^{+28}_{-16}

* E-mail: ethan.winch@armagh.ac.uk

M_{\odot} . One explanation for these high masses would be that these heavy BHs inside the traditional PI gap are themselves the product of earlier merging (Fishbach & Holz 2020; Fragione et al. 2020; Romero-Shaw et al. 2020; Renzo et al. 2020b), but alternatively the assumptions in the stellar evolution considered up to that point in time was incorrect or incomplete. One possible solution would be that the nuclear reaction rates, in particular the $^{12}\text{C}(\alpha, \gamma)^{16}\text{O}$ nuclear reaction rate is uncertain (Takahashi 2018; Farmer et al. 2020), but even using standard nuclear reaction rates there might be a solution from a stellar evolutionary viewpoint. The key physical points are, on the one hand, to avoid entering the PI physics regime, maintain a sufficiently small core, and on the other hand to simultaneously retain a sufficiently large H envelope, both of which are possible for massive stars at reduced Z (Vink et al. 2021), where it was shown that a blue supergiant (BSG) can maintain a sufficiently large H envelope to produce an $85 M_{\odot}$ heavy BH as long as the amount of core overshooting ($\alpha_{\text{ov}} \leq 0.1$) is small (see the full motivation in Sect. 2.2). Note that such a configuration of a small core and large Hydrogen envelope can also be produced in stellar mergers. Spera et al. (2019) and Di Carlo et al. (2019) found this to be a possibility using binary population synthesis, but single star models did not produce a BH over $60 M_{\odot}$ in their set-up.

While we now know that such BSG models might potentially explain the mere existence of such heavy BHs (see also Tanikawa et al. 2021; Costa et al. 2022) in the traditional second mass gap (even without invoking mergers, second generation events, or nuclear physics adaptations) we still do not know the theoretical stellar upper BH mass limit before PI, nor do we know exactly which ZAMS mass would be able to produce this upper BH mass. Furthermore, while extreme $85 M_{\odot}$ cases are exciting, due to the shape of the initial mass function (IMF) we would normally expect larger numbers of BHs to be found just above the $50 M_{\odot}$ BH/PI boundary, than towards the $90 M_{\odot}$ upper end.

For these reasons, we set out to compute a significantly expanded (compared to Vink et al. (2021)) grid of massive star models, to map the initial ZAMS masses into final masses (and related BH masses) due to stellar evolution assumptions of stellar interior mixing (core overshooting, rotation, semi-convection) and exterior stellar wind physics as a function of Z . We first set out to determine the lower boundary of the PI region (Fowler & Hoyle 1964; Barkat et al. 1967; Woosley 2017; Farag et al. 2022). The upper boundary of the PI mass gap is estimated at $M_{\text{ZAMS}} \sim 130 M_{\odot}$ (Bond et al. 1984; Heger et al. 2003; Farag et al. 2022). Stars above this value are predicted to direct collapse to a black hole. However, as these stars are above the PI mass gap, they are not considered in this work.

The lower boundary of the PI mass gap, where PI physics takes place, had previously been estimated to occur at masses of $50 M_{\odot}$, such as Woosley (2017) or Farmer et al. (2019) for pure helium stars. The H-rich situation was explored in Vink et al. (2021), where a star of mass similar to the primary component of GW 190521 retained almost all of its hydrogen (H) envelope into the final stages of its life, avoiding pair instability. The current work systematically continues the study of heavy BHs from stars in the traditional PI gap by exploring a much broader parameter space, allowing us not only to investigate which model parameters produce the heaviest BHs, but also how often this could occur, and what is the relative likelihood of the heaviest BHs in comparison to heavy BHs at the lower PI gap boundary. While these results are interesting for comparison to special features in GW data, isolated BHs could potentially also be tested by methods such as microlensing (Lam et al. 2022).

Section 2 explores our implementation of stellar parameters in MESA. Section 3 determines values for the critical core masses

(herein referred to as the M_{crit} Experiment), while Section 4 explores the entire model grid and parameter space to verify which parameters produce the maximum BH mass (herein referred to as the Main Grid). In Section 5, we derive analytic fits to our data in the form of two equations. Section 6 provides context to our work in terms of a BH distribution per initial mass. Section 7 provides discussion in the context of other work in the community, and Section 8 presents our summarised conclusions. Appendix A presents a list of all 336 models and their input parameters, while Appendix B details the resolution test conducted before running the grid. Appendix C discusses the critical rotation rate in the context of informing future work, Appendix D discusses our choice of mass loss rates, and Appendix E discusses the effect of MLT++ at low metallicity and on the maximum black hole mass.

2 METHODS

In this paper, we perform detailed stellar evolution employing a two-pronged strategy. First, we run a limited set of models all the way until end of core oxygen burning (unless they enter PI first) to establish whether the mass of the Carbon-Oxygen core (or He core) – that sets the boundary between a model which undergoes PI and a model which does not (the *critical* core mass) – is constant across our parameter space (in terms of α_{ov} etc.). This forms our M_{crit} experiment models. If they are, then as a second step the critical core mass can be robustly employed to run a larger grid of 336 models just until the end of core Helium burning, as at this point both the Helium and Carbon-Oxygen cores will have been established. This forms our main grid.

The aim of this study is to derive the final masses, M_{final} , from detailed stellar evolution models, and we do not study the 3D hydrodynamical collapse that creates a BH. For this latter part of BH formation we will rely on the work of others (e.g. Fernández et al. 2018). In other words, our strategy is to derive accurate final masses (M_{final}) from detailed stellar evolution modelling to provide a distribution on BH masses, and in particular on the maximum BH mass below PI. We will come back to this issue in the Discussion of Section 7.

2.1 MESA Modelling

We use MESA version r15140 (Paxton et al. 2011, 2013, 2015, 2018, 2019) to evolve the main grid of 336 stellar evolution models from ZAMS to core Helium exhaustion, as well as a subset of models extending beyond Helium exhaustion and into core Oxygen burning (the M_{crit} Experiment), the details of which are further discussed in Section 3 and shown as part of the results in Section 4.

We include the standard Mixing Length Theory (MLT) of convection by Cox & Giuli (1968) with an $\alpha_{\text{MLT}} = 1.82$ as in Choi et al. (2016). We employ the Ledoux criterion for convective stability with a varying efficiency parameter described in Section 2.2. During core He burning, massive stars evolve as supergiants with massive convective envelopes where radiative transport can become important. Supra-Eddington conditions can be realised locally inside the star in the regions of strong opacity bumps with structure models predicting strong inflation and density inverted layers on top to maintain hydro-static equilibrium. We note that the 1D treatment of radiative envelopes is an unsolved problem in Astrophysics (Ishii et al. 1999; Petrovic et al. 2006; Gräfenor et al. 2012; Jiang et al. 2015; Grassetelli et al. 2021; Gilkis et al. 2021; Klencki et al. 2021; Romagnolo et al. 2022) Some stellar models, such as BEC, allow inflation to

occur (e.g. Köhler et al. 2015), while other models such as GENEC and MESA avoid the inflation and density inversion effects, either by swapping the density and pressure scale heights, enhancing mass loss in supra-Eddington layers (e.g. Ekström et al. 2012), or boosting convective energy transport efficiency employing MLT++ in MESA.

The models of our main grid employ MLT++, as this is necessary for such high mass models to evolve into later stages of evolution (post-TAMS). This is required to avoid convergence issues in the envelopes resulting from density inversions in the outer layers where inefficient convective zones lead to radiation dominant regions. As for physical effects, MLT++ makes the star evolve hotter, and more compact. Calibration of the MLT++ parameters based on the red supergiant luminosity cutoffs in the Galaxy and the Magellanic Clouds is detailed in Sabhahit et al. (2021), while the description of how MLT++ is implemented is provided in Paxton et al. (2013). For our grid, we use the default parameter values of MLT++ across the main grid models but showcase a model without MLT++ at very low metallicity in Appendix E.

We include the effects of rotational mixing in our models, and therefore we implement the following instabilities; Solberg-Hoiland, Secular Shear Instability, Eddington-Sweet circulation and Goldreich-Schubert-Fricke, following (Heger et al. 2000). The multiplicative diffusion factors to the diffusion coefficient of these different rotation-induced instabilities are all set to unity. The rotational component of the diffusion coefficient for mixing of material is multiplied by a factor $f_c = 1/30$ (AM_D_MIX_FACTOR in MESA). The sensitivity of the rotation induced mixing to the composition gradient is controlled by the f_μ parameter which is set to 0.05 (AM_GRADMU_FACTOR in MESA). Both these values follow Heger et al. (2000).

For our wind prescription, we follow Vink et al. (2021) and modify the MESA "Dutch" wind, which is a collection of wind recipes from Vink et al. (2001), de Jager et al. (1988), and Nugis & Lamers (2000). For our modified Dutch recipe we will use Vink et al. (2001), with a redefined Z dependence such that it is dependent on Z_{Fe} as opposed to the total metallicity in the Z term. However, if the star drops below a certain temperature ($T_{\text{eff}} < 4\text{kK}$), the model then switches to de Jager et al. (1988). If the surface Hydrogen abundance drops below 0.4 with a surface temperature of $T_{\text{eff}} > 50\text{kK}$, then the star is considered a Helium-rich Wolf-Rayet (WR) and uses the recipe of Nugis & Lamers (2000).

As there are few observational constraints on mass-loss rates from massive stars in our parameter regime, there is notable uncertainty in stellar evolution modelling. For instance, a more appropriate WR recipe could be the recent theoretical one from (Sander & Vink 2020), but as the bulk of our models remain cool, they do generally not enter this regime. More pressing questions would concern the absolute mass-loss rates during core H burning, where stars spend 90% of their lives, and whether our models could encounter a phase of elevated mass-loss, due to becoming optically thick (Vink & Gräfener 2012). Regarding the former, for canonical massive stars there is uncertainty in the mass-loss rates by a factor 2-3 (Vink 2022; Björklund et al. 2021; Krtićka & Kubát 2017). However absolute mass-loss rates have only been calibrated at the higher $\sim 80 M_\odot$ range (Vink & Gräfener 2012). Alternative recipes such as Björklund et al. (2021) do not appear to provide the more appropriate higher rates in this transition regime, and we thus refrain from lowering mass-loss rates. Having noted this, as we are in the low Z regime and H-burning mass-loss rates are modest, this choice would not affect the results. Regarding the issue of mass-loss enhancement in close proximity to the Eddington limit (Vink et al. 2011), we have recently included this in MESA models (Sabhahit et al. 2022, 2023), and as we show in Appendix D and Fig. D1, the models in our grid are not in this

regime. On the specific issue of luminous blue variable (LBV) mass loss (Grassitelli et al. 2021), we refer the reader to Sect. 4.1 in (Vink et al. 2021) for a discussion. In short, we cannot guarantee that LBV type mass loss would play some role, but it is unlikely due to the lower Z (Kalari et al. 2018). As we estimated in Vink et al. (2021) (see their Sect. 4.1), we could expect a total loss of $0.19 M_\odot$ over the entire duration post core He-burning. This value is comparable to the amount of mass lost during core collapse and negligible in the context of our overall assumptions. In any case, if mass loss was stronger (and/or envelope inflation more pronounced) then this could affect the Z-dependent cut-off on the maximum BH, as discussed in Vink et al. (2021) and shown in Figure 3 of that paper. It would however have no effect on the BH maximum at low Z itself, which is therefore a robust number in the mass-loss context, as discussed in Vink et al. (2021).

For the spatial meshing of the model during mass adjustment, the MESA code employs an inner Lagrangian meshing (constant m) and a homologous meshing (constant $q = m/M$) in the envelope (Paxton et al. 2011, 2015). To facilitate a smoother run of our full model grid till end of evolution, we employ a deeper location for the switch from a Lagrangian meshing to a homologous meshing. A side effect of using such a deeper homologous mesh is that the models take larger timesteps during the main sequence ($dt \approx 10^4$ years as opposed to $\approx 10^2$ without a deeper homologous mesh). Thus an additional timestep control limiting the model to a maximum timestep of 10^3 years is used which allows us to properly resolve thermally unstable layers, mainly semiconvective layers. The usage of the maximum timestep control also has the effect of limiting timesteps during short phases beyond core He burning, which allows models in the critical core mass experiment (Section 3) to complete oxygen burning. For further information on spatial and timestep meshing, see Appendix B.

2.2 Parameter Space

For our study we are interested in physical parameters which affect the evolution of the star at low Z. These are parameters which either have a significant effect on the core size, or affect the final mass of the star. For this we vary initial mass, initial metallicity up to Small Magellanic Cloud (SMC) $Z_{\text{SMC}} = 1/5 Z_\odot$, core overshooting, rotation, and semiconvection. We do not vary the $^{12}\text{C}(\alpha, \gamma)^{16}\text{O}$ reaction rate, instead opting to maintain the standard rates for the course of our grid, as we wish to focus on stellar evolution uncertainties. A brief discussion on uncertain $^{12}\text{C}(\alpha, \gamma)^{16}\text{O}$ reaction rate can be found in Section 7.

The final mass from stellar modelling can be constructed by considering the stellar core versus the envelope:

$$M_{\text{final}} = M_{\text{core}}(M_{\text{ZAMS}}, \alpha_{\text{ov}}, \Omega/\Omega_{\text{crit}}) + M_{\text{envl}} \quad (1)$$

Where M_{core} is the mass of the star's core, and M_{envl} is the mass of the star's envelope above the core. Both parameters are functions of our entire parameter space, however there are parameters which have a higher degree of impact to each part. M_{core} is predominantly a function of ZAMS mass, amount of core overshooting and rotation, while M_{final} is predominantly governed by M_{ZAMS} and Z which affects M_{envl} . In Section 5, we define explicit equations to these parameters and their relationship. For our grid of models, we focus on five parameters which can potentially drastically affect the evolution of a very massive star (we discuss other parameters in Section 7). These parameters are initial mass (M_{ZAMS}), metallicity (Z), overshooting (α_{ov}), rotation ($\Omega/\Omega_{\text{crit}}$), and semiconvection (α_{sc}).

Initial mass is the mass of the star at the Zero-Age Main Sequence (ZAMS) and is the first factor in determining the potential BH mass, as it provides an upper limit. Our mass range includes the values; 60, 80, 90, 100, 110, 120, 150 M_{\odot} .

Initial metallicity refers to the abundance of elements other than Hydrogen and Helium, but crucially Iron, in the star at the ZAMS point, and is an important factor in the evolution of a massive star due to metallicity dependent winds. As we scale our abundances according to [Grevesse & Sauval \(1998\)](#), all values of metallicity we use are given as fractions of Solar metallicity (Z_{\odot}). We define abundances according to three initial mass fractions, $Z_{\odot} = 0.02$. The initial helium mass fraction in our models is evaluated as follows: $Y = Y_{\text{prim}} + (\Delta Y/\Delta Z) \times Z$ using MESA default values of $Y_{\text{prim}} = 0.24$ and $(\Delta Y/\Delta Z) = 2$. This leaves the hydrogen mass fraction (X) defined from unity, where $X + Y + Z = 1$. We also apply this metallicity value to the OPAL Opacity tables from [Rogers & Nayfonov \(2002\)](#). Our metallicity values range from $Z = 10^{-3} Z_{\odot}$ to $Z_{\text{SMC}} = 0.004$.

Convective boundary mixing (CBM) is a fluidic phenomenon which occurs above and below convective regions in stars ([Langer 2012](#); [Anders & Pedersen 2023](#)). Regions of convection in stars are determined by the Schwarzschild equation, however fluid packets rising or falling to this boundary can still overshoot the boundary, thus creating a region of extra mixing above and below convective regions. As this is a 3-dimensional phenomenon, it is not possible to fully represent this in 1-dimensional stellar evolution, however CBM can have a dramatic effect on the evolution of a model ([Higgins & Vink 2019](#); [Vink et al. 2021](#)). For our models, we use "step" overshooting. Step overshooting assumes a solid block of extra mixing, with the length or height predetermined by α_{ov} which is a fraction of the pressure scale height, H_p .

Appropriate values to be used for CBM are highly uncertain. Up to 2010, most massive star evolution modellers employed relatively small values (of order $\alpha_{\text{ov}} = 0.1$), but in order to accommodate the presence of B supergiants and an extended width of the main sequence, [Vink et al. \(2010\)](#) suggested that overshooting values up to $\alpha_{\text{ov}} = 0.5$ should be considered. Such an increased amount of overshooting with stellar mass has also been employed by [Bressan et al. \(2012\)](#); [Claret & Torres \(2016, 2017\)](#); [Constantino & Baraffe \(2018\)](#); [Scott et al. \(2021\)](#). However, this is only part of the story, as asteroseismology studies of B stars in the 10-20 M_{\odot} range [Bowman \(2020\)](#) indicate a roughly equal distribution for low ($\alpha_{\text{ov}} \leq 0.1$, [Dupret et al. \(2004\)](#)) and high ($\alpha_{\text{ov}} \simeq 0.44$; [Briquet et al. \(2007\)](#)) values. Future asteroseismology ([Aerts et al. 2019](#)) is needed to study CBM for higher mass objects. The origin for what may be the root cause for the spread of CBM values per mass bin remains to be understood ([Costa et al. 2019](#); [Higgins & Vink 2023](#)). Meanwhile, our strategy in constructing stellar models has been to consider both low ($\alpha_{\text{ov}} = 0.1$) and high ($\alpha_{\text{ov}} = 0.5$) values for massive OB stars ([Higgins & Vink 2019, 2023](#)). For these reasons, our adopted values here are similar: $\alpha_{\text{ov}} = 0.1, 0.3, 0.5$. We limit overshooting to only occur above the core, the same value of which is implemented through to Carbon depletion for M_{crit} experiment models, or to Helium exhaustion for the main grid.

Stellar rotation is a powerful factor in massive star evolution (for a review of which, see [Maeder & Meynet \(2000a\)](#)), able to induce chemical mixing and lead to large amounts of mass loss if a star is supercritical such as in [Meynet et al. \(2006\)](#). Thus, rotation can also enhance the effects of, and also be affected by, other parameters such as Z -dependent winds. For our models, we use rotation as a fraction of the critical breakup speed ($\Omega/\Omega_{\text{crit}}$), as we want to maintain the same rotational effects between ZAMS masses. Our values of rotation in our main grid (Section 4) are $\Omega/\Omega_{\text{crit}} = 0.2, 0.4$

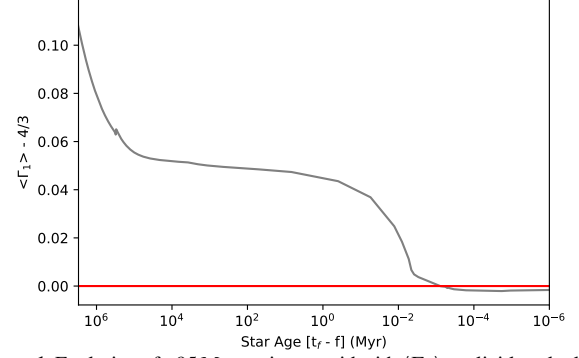


Figure 1. Evolution of a $95 M_{\odot}$ star in our grid with $\langle \Gamma_1 \rangle$ explicitly calculated. The red line denotes where a star may become pair unstable by reducing below that point. The $\langle \Gamma_1 \rangle$ is normalised to 0 in this case. The horizontal axis follows the evolution of a star in logarithmic time until the end of the model. This allows us to see the evolution of $\langle \Gamma_1 \rangle$ across the life of the star, and clearly show the last period of the star's life, where $\langle \Gamma_1 \rangle$ drops below $4/3$.

which corresponds to surface rotation rates of $\sim 150, 300 \text{ km s}^{-1}$ (as motivated by observed rotation rates for O stars at low Z [Ramírez-Agudelo et al. 2013](#); [Sabín-Sanjulián et al. 2017](#); [Ramírez-Agudelo et al. 2017](#); [Ramachandran et al. 2019](#)). For our M_{crit} experiment and our main grid, we do not use rotation enhanced mass loss ([Müller & Vink 2014](#)). However, in Appendix C we discuss the specific case of high rotation.

The last parameter we vary is semiconvective efficiency. Semiconvection, first discussed in [Kato \(1966\)](#), applies to a region above the core of a star during the Main Sequence, where there is slow mixing of chemical elements. We use the Ledoux criterion to determine regions of semiconvection and full convection. A region is convectively unstable if Equation 2 is fulfilled, while it is semiconvective if Equation 3 is fulfilled.

$$\nabla_{\text{ad}} + \frac{\phi}{\delta} \nabla_{\mu} < \nabla \quad (2)$$

$$\nabla_{\text{ad}} < \nabla < \nabla_{\text{ad}} + \frac{\phi}{\delta} \nabla_{\mu} \quad (3)$$

where ∇ is the temperature gradient, ∇_{ad} is the adiabatic temperature gradient, and ∇_{μ} is the chemical gradient. ϕ and δ are the density gradients with respect to temperature and mean molecular weight respectively. Semiconvection can be seen above the core during H burning, as the core retreats, leaving behind said chemical gradient. However, the largest effect on a star's evolution from semiconvection happens during the post-MS phases, and can affect the temperature of the model, and the presence and duration of "blue loops" ([Langer 2012](#)).

2.3 Pair Instability

The PI region, from [Fowler & Hoyle \(1964\)](#), is due to production of electron positron pairs in the core of a very massive star, leading to a reduction in the pressure component of the equation of state, and thus the gravitational contraction of the star. This leads to explosive oxygen burning, and can result in either a partial or complete explosion depending on the location of the instability. In the event of a partial explosion, large amounts of stellar material can be thrown off at once, forming a Pulsational Pair Instability Supernova (PPISN)

(Barkat et al. 1967; Woosley 2017). Alternatively, the star can be completely disrupted, and the resulting Pair Instability Supernova (PISN) leaves no compact remnant (Barkat et al. 1967; Farag et al. 2022).

The boundary for where PI or PPI occurs is a debated topic, for example Farmer et al. (2019), Costa et al. (2022) and Volpato et al. (2023), as such several criteria are used to determine whether a star becomes pair unstable or not. Principally, the first criterion is that spontaneous pair production occurs in the star. For this to happen, the star needs to be massive enough such that the internal temperature reaches a point where a sufficiently large number of photons in the high energy tail of the Planck function have energies in excess of the rest mass. While this condition can be used as a diagnostic for PI, and can be visualised on a Temperature-Density diagram, alternatively one can instead use the size of Helium or Carbon-Oxygen cores as a determining factor. This has the benefit of providing a comparable diagnostic factor to determine the PI boundary.

For calculating which models became pair unstable, we calculated the average Γ_1 (see Equation 5) across the entire star at each timestep. As our current models do not include any implicit Hydrodynamics, we only split our model according to whether or not they became pair unstable at all ($\langle\Gamma_1\rangle < 4/3$).

An example of our calculation of $\langle\Gamma_1\rangle$ across the evolution of a stellar model is presented in Figure 1, showing a model which would undergo some form of Pair Instability.

The equation for Γ_1 is given in Equation 4.

$$\Gamma_1 = \left(\frac{d \ln P}{d \ln \rho} \right)_{\text{ad}} \quad (4)$$

While it is possible to calculate the value of $\langle\Gamma_1\rangle$ for each model, it is also not necessary. As seen in Farmer et al. (2019) and Farmer et al. (2020), it is possible to determine which models will undergo Pair Instability based on the mass of their Carbon-Oxygen or their Helium core mass (see Section 3). As such, the majority of the grid can be categorised based on both of these criteria. For the M_{crit} experiment models which are used to calculate the critical core masses, some of these models do not deplete Oxygen, but all models are core Carbon depleted. Similar to Farmer et al. (2020); Costa et al. (2021), we use the following equation to calculate the average Γ_1 across our stellar model:

$$\langle\Gamma_1\rangle = \frac{\int \Gamma_1 P d^3 r}{\int P d^3 r} \quad (5)$$

from Stothers (1999), who shows that this is a good approximation for determining the dynamical stability of the star. When the $\langle\Gamma_1\rangle$ of a star would fall below $4/3$, PI would occur which causes the dynamical instability. As this is an approximation, this does not inform as to the location of the PI within the star, and as such only informs us that PI occurs, not whether the star would undergo Pulsational Pair Instability or full disruption (i.e. PISN).

In the following Section 3, we use this equation and stellar evolution models to demonstrate that the critical CO and Helium core masses are robust, and that therefore we use the core masses as our criteria for the PI boundary.

3 M_{CRIT} EXPERIMENT

The critical core mass is the mass of the stellar core such that the integral of the adiabatic index, $\langle\Gamma_1\rangle$, drops below $4/3$. In this case, the model will undergo PI, such as in Farmer et al. (2019). This will

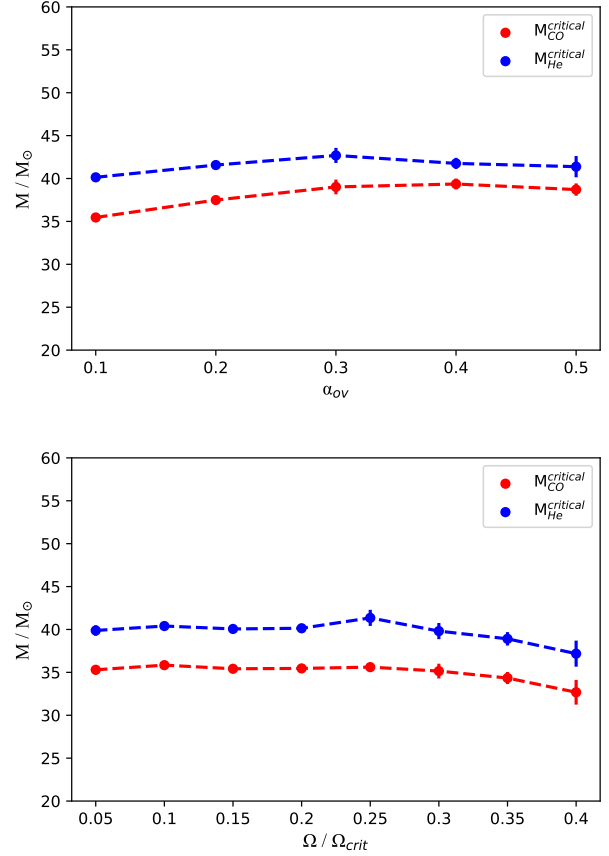


Figure 2. Critical core mass values for Helium ($M_{\text{He}}^{\text{critical}}$) and CO ($M_{\text{CO}}^{\text{critical}}$) when varying α_{ov} (top panel) and $\Omega/\Omega_{\text{crit}}$ (bottom panel). Each data point represents the median between two models which straddle the PI boundary. The difference between these models' M_{CO} and M_{He} values provides us with an error bar, which is small enough to be hidden behind the data points on these graphs.

be achieved with a critical mass for the Helium and Carbon-Oxygen cores, which has been shown in previous work to be an effective diagnostic for this purpose (Farmer et al. 2019; Costa et al. 2021). This section will provide values of the critical core masses with which we can apply to the main grid in Section 4 and to our population in Section 6.

To do so, we use the model A1 ($M_{\text{ZAMS}} = 90 M_{\odot}$, $Z = 1/10$ th Z_{\odot} , $\alpha_{\text{ov}} = 0.1$, $\Omega/\Omega_{\text{crit}} = 0.2$, $\alpha_{\text{sc}} = 1$) from Vink et al. (2021) as a starting point, as this is known to already be close to the BH/PI boundary. Then, we isolate one parameter (M_{ZAMS} , Z , α_{ov} , $\Omega/\Omega_{\text{crit}}$, α_{sc}) which we vary, and evolve the models until Oxygen depletion. This provides an indication if the model undergoes PI, and thus allows us to map the PI limit for that parameter.

In Figure 2, we show our calculated critical core mass across different values of overshooting (top panel) and rotation (bottom panel) for $M_{\text{CO}}^{\text{critical}}$ and $M_{\text{He}}^{\text{critical}}$. Stars that have core masses which are on or below their respective line will avoid Pair Instability, while those above undergo PI.

The ZAMS mass of the star corresponding to the critical core mass can be seen to vary in the yellow-shaded region of the bottom panel of Figure 3. This figure combines the critical Helium core mass of Overshooting, Rotation and Semiconvection in the top panel, and provides the corresponding ZAMS masses in the bottom panel. As

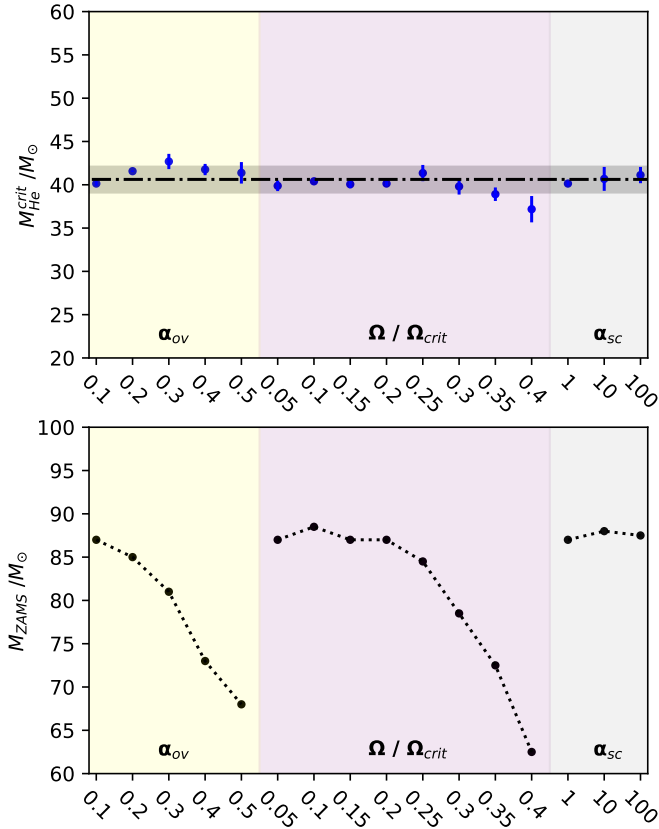


Figure 3. The top panel shows the critical core mass for Helium varying across 3 parameters - α_{ov} , Ω/Ω_{crit} , and α_{sc} . The average of these values - $40.6 M_{\odot}$ - is shown with the black dash-dot line, which we use as our fiducial critical Helium core mass ($M_{He}^{critical}$) throughout the paper. The black shaded region is our uncertainty, which represents the standard deviation of $M_{He}^{critical}$. The bottom panel shows corresponding ZAMS masses for the value of $M_{He}^{critical}$.

established, the critical core mass remains constant when varying α_{ov} , as this does not change the density of the core. Instead, increasing or decreasing α_{ov} has the effect of increasing or decreasing the total mass of the core. Thus, for the same corresponding Helium core mass, the ZAMS mass of the star will be inversely proportional to the amount of overshooting, α_{ov} .

Regardless of variation in M_{ZAMS} with α_{ov} , Ω/Ω_{crit} , or α_{sc} , the critical core mass is more or less constant. This critical core mass will be used in our determination of whether a model undergoes PI or not.

By taking the average of each parameter's critical core mass boundary, and then averaging those values, we arrive at a critical CO core mass boundary of $M_{CO}^{critical} = 36.3 \pm 1.8 M_{\odot}$ and critical Helium core mass boundary as $M_{He}^{critical} = 40.6 \pm 1.5 M_{\odot}$. Formal uncertainties are the combination of the standard deviations from the critical core masses in α_{ov} , Ω/Ω_{crit} , and α_{sc} . The critical Helium core mass boundary is shown in the top panel of Figure 3, where regions are shaded depending on varying parameter (yellow for overshooting, light pink for rotation and grey for semiconvection).

To summarise, we have tested the role played by overshooting, semiconvection and rotation in setting the lower PI boundary limit by the critical core mass. We obtain the critical CO mass and critical

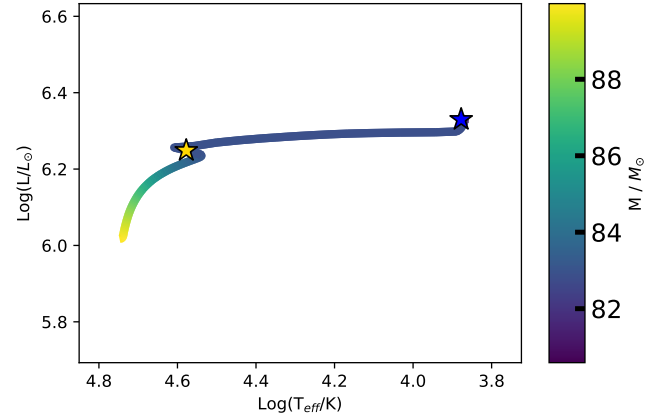


Figure 4. Hertzsprung-Russell diagram of a model with $M_{ZAMS} = 90 M_{\odot}$, $Z = 1/10$ th Z_{\odot} , $\alpha_{ov} = 0.1$, $\Omega/\Omega_{crit} = 0.2$, and $\alpha_{sc} = 1$. The gradient colour of the track illustrates the mass of the star. The gold and blue stars reflect the points of core Hydrogen and core Helium exhaustion respectively.

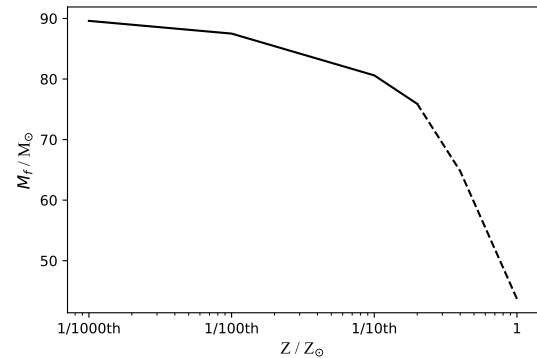


Figure 5. Final mass of models varying with metallicity. These models start with $90 M_{\odot}$ and vary from Solar metallicity to 1/1000 th Solar metallicity. Stars which are above the dotted line represents metallicities above that of the SMC, which are beyond our grid.

The core mass of described in the above paragraph. More crucially, we find *the critical core boundaries do not vary systematically with either overshooting, semiconvection, or rotation* within our parameter space. Such a critical core mass criterion remains independent of processes that can alter the core size and is a robust condition to determine the fates of our models.

4 MAIN MODEL GRID

In this section, we detail our grid of 336 models, describe the statistics of the grid, and discuss several features. Our parameter space is detailed in Table 1. A breakdown of each model in the model grid can be found in Appendix A. The main grid of models was calculated to the end of Helium burning, and then the Carbon core mass taken and compared with the critical $M_{CO}^{critical}$ from Section 3. An example of our models is shown in Figure 4, for a $M_{ZAMS} = 90 M_{\odot}$ model.

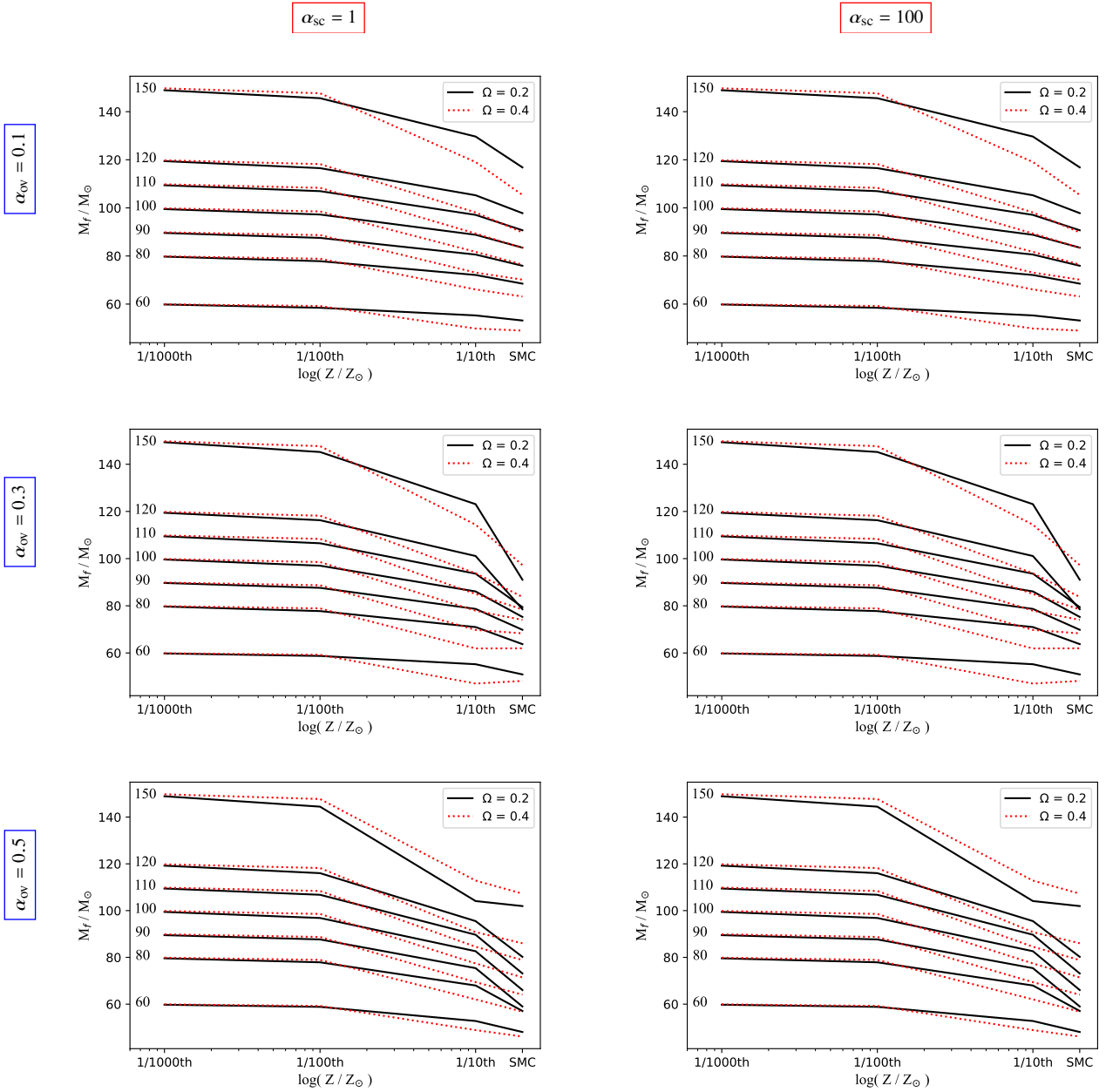


Figure 6. Final masses of stars as a function of metallicity. Low rotation ($\Omega/\Omega_{\text{crit}} = 0.2$) models are shown with the black solid line, while the higher rotation ($\Omega/\Omega_{\text{crit}} = 0.4$) models are represented with the red dotted line. Models with $\alpha_{\text{sc}} = 1$ are shown in the left column. Models with $\alpha_{\text{sc}} = 100$ are shown in the right column. Each row is divided by α_{ov} in descending order. Kinks in the curve can be found at SMC metallicity due to the presence of the bi-stability jump in the wind physics. The final mass of high rotation models at low metallicity are likely overestimated due to the lack of a supercritical rotation mass loss recipe.

M_{ZAMS}	Z/Z_{\odot}	α_{ov}	$\Omega/\Omega_{\text{crit}}$	α_{sc}
60	1/5	0.1	0.2	1
80	1/10	0.3	0.4	100
90	1/100	0.5		
100	1/1000			
110				
120				
150				

Table 1. Detailed list of parameters used in our model grid. We provide the initial mass (M_{ZAMS}), metallicity (Z), overshooting parameter (α_{ov}), rotation rate as a function of critical rotation ($\Omega/\Omega_{\text{crit}}$), and semiconvective efficiency parameter (α_{sc}).

4.1 Key Parameters of the Main Grid

Metallicity is one of the key parameters of the main grid. Figure 5 shows the effect of metallicity as a function of solar metallicity on the final mass of the star at the end of Helium burning. Below $1/10\text{th } Z_{\odot}$, the mass loss is negligible (less than 10% of total mass), however the function steepens as the models increase to SMC and Large Magellanic Cloud (LMC) metallicity, then finally Z_{\odot} where the mass loss is non-negligible. A summary of the main grid of results is presented in Figure 6. Immediately noticeable is the effect of metallicity on the final mass of a model. For models at Z_{SMC} , mass loss is non-negligible and is a significant ($\dot{M}_{\text{Total}} > 10\%M_{\text{ZAMS}}$) percentage of the star's mass. At $1/10\text{th } Z_{\odot}$, the mass loss becomes

considerably weaker. At this metallicity, the stars retain the majority of their envelope through their evolution. This also means that the other parameters (such as overshooting, as shown in Section 5, and can be seen in the columns of Figure 6) become a lot more important for determining the mass of a BH, as these parameters will affect the core size. For very low metallicities ($Z \leq 1/100\text{th } Z_{\odot}$), the mass loss becomes negligible, with an average mass loss of $< 2 M_{\odot}$.

As discussed in Section 3, the core mass must be kept below $M_{\text{CO}}^{\text{critical}} < 36.3 \pm 1.8 M_{\odot}$ or $M_{\text{He}}^{\text{critical}} < 40.6 \pm 1.5 M_{\odot}$ in order to avoid pair instability phenomena.

As can be seen in the bottom panel of Figure 3, the ZAMS mass at which the a star would undergo PI is an inverse function of α_{sc} . See Section 3 for discussion on the interaction between M_{ZAMS} , $M_{\text{core}}^{\text{critical}}$, and α_{ov} . This indicates a strong correlation between these two parameters which is well defined in Section 5. For our values of rotation corresponding to ZAMS mass in the bottom panel Figure 3, we see that larger values of $\Omega/\Omega_{\text{crit}}$ correspondingly decrease the maximum value of initial mass that a model can have before it becomes pair unstable.

4.2 Features of Rotation and Semiconvection in the Main Grid

Rotation becomes important at very low metallicity ($Z \leq 1/100\text{th } Z_{\odot}$). At these metallicities, the wind mass loss is low enough such that models may spin up and reach critical breakup speed due to an inability to lose sufficient angular momentum during the main sequence. For models with which $Z = 1/100\text{th } Z_{\odot}$, and with initial $\Omega/\Omega_{\text{crit}} = 0.4$ reached critical breakup speed before core helium exhaustion, whereas models with initial $\Omega/\Omega_{\text{crit}} = 0.2$ would remain sub-critical during their evolution. However, at $1/1000\text{th } Z_{\odot}$, all models spun up to critical breakup speed in their lives. Conversely, at $1/10\text{th } Z_{\odot}$, all models were able to reach the end of core Helium burning without spinning up to breakup speeds.

This is due to mass loss via winds being an important mechanism for dumping angular momentum from the star. For models with $Z \geq 1/10\text{th } Z_{\odot}$, the winds were able to eject enough angular momentum such that, even in the high rotation case, the stars did not reach breakup speeds. This relationship demonstrates a metallicity-dependent value of $\Omega/\Omega_{\text{crit}}$ which acts as a bifurcation point - values of rotation above this value critically spin up, and values below this are able to evolve without reaching critical rotation rates.

A sketch of where this value lies is shown in Figure 7, where the red region denotes a star which will spin up such that $\Omega/\Omega_{\text{crit}} > 1$, and therefore breakup. Whereas stars in the blue region are able to spin down or lose angular momentum such that their maximum rotation value remains below breakup speed. At SMC metallicity and greater, the strength of the mass loss would likely be enough for the star to lose most of its angular momentum regardless of initial rotation rate. It is interesting to note that, within our mass range, this feature is not mass dependent.

This feature is important to the evolution of massive stars in the black hole/pair instability formation scenarios as this has a direct effect on the likelihood of formation for either scenario, as well as the mass distribution of black holes or PPISN/PISN progenitors. For models which have low rotation at the ZAMS, a relation exists where lower metallicity increases the maximum possible BH mass. However, by increasing rotation, this relationship changes due to large, episodic, mass loss at a cutoff metallicity - this cutoff is shown by the red line in Figure 7. Below this cutoff, stars will experience episodes of rotationally induced mass loss which will lower their maximum BH mass, potentially on the order of tens of solar masses

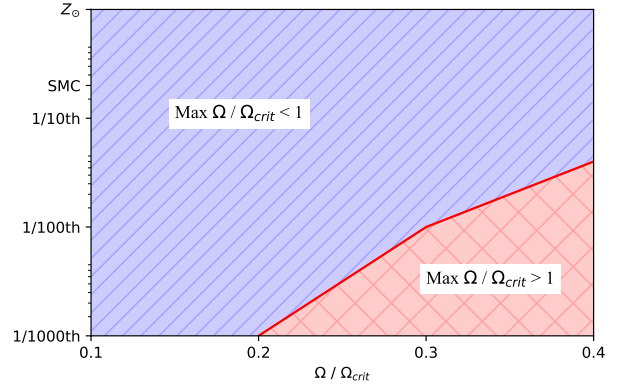


Figure 7. Sketch of relationship between metallicity and maximum $\Omega/\Omega_{\text{crit}}$ across the entire evolution. Stars which have initial rotation values in the red region would not lose enough angular momentum via mass loss, leaving them to become supercritical when they contract and thus experience a period of very high mass loss. Above a certain metallicity, the initial rotation rate becomes irrelevant as the mass-loss rates are always substantial enough to shed enough angular momentum.

(Meynet et al. 2006). Further discussion on high rotation at low metallicity is presented in Appendix C.

Overall, rotation can have various effects on the evolution and fate of a star. In addition to the episodic mass loss caused by rapid rotation as in Meynet et al. (2006), there is also the adjustment to the Γ_1 criterion as in Marchant & Moriya (2020) (which has a noticeable effect from $\Omega/\Omega_{\text{crit}} \geq 0.3 - 0.4$), as well as chemically homogeneous evolution (Yoon & Langer 2005). The combined effects of these three rotational phenomena is beyond the scope of this Paper, and is a topic for future studies.

Semiconvection is the weakest parameter in this study. At high values of initial mass, factors such as overshooting and rotation will dominate the effects of semiconvection to the point where models with weak or strong semiconvection are indistinguishable. At our lowest masses ($M_{\text{ZAMS}} = 60 M_{\odot}$), regions of semiconvection do become more prominent. However, this does not seem to affect the final fate of the model in any systematic way across our parameter space, except for isolated cases in CO core size.

For any indirect effect on mass loss, semiconvection was not noted to have a dominant effect here either. Temperature differences were typically small enough (nominally $< 0.1 \text{ dex}$), or occurred for short timescales such that mass loss was almost the same between models of the same parameter space, and different α_{sc} .

Semiconvection does not directly affect the size of the core. The primary effect is instead related to the temperature of the model and this is mostly constrained to the post-TAMS environment, where longer blue-loops can occur for stars with $M_{\text{ZAMS}} = 20 - 30 M_{\odot}$ (Langer et al. 1985). In Figure 8, we can see the difference between high efficiency semiconvection for a $90 M_{\odot}$ model ($\alpha_{\text{sc}} = 100$, subfigure 8b) and low efficiency ($\alpha_{\text{sc}} = 1$, subfigure 8a). The semi-convective efficiency shifted the TAMS temperature of the high efficiency model to be 0.1 dex cooler. The red regions in the Kippenhahn diagrams of Figure 8 denoting regions of semiconvective mixing become much more prominent with lower efficiency. This was not seen to have a significant effect on the evolution of the model, or the location of the PI limit.

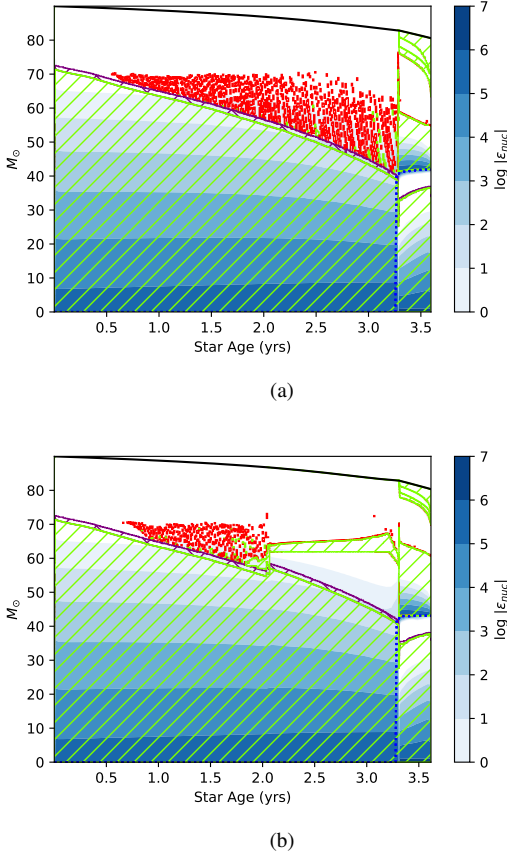


Figure 8. Stellar structure diagrams for a $90 M_{\odot}$ model with $\alpha_{sc} = 1$ (Figure 8a), and $\alpha_{sc} = 100$ (Figure 8b). Fully convective regions are marked by green hash, while semiconvective regions are marked with red fill. Overshooting regions are seen in purple, and the Helium core mass is bounded by the blue dotted line. Blue shading indicates regions of nuclear burning.

4.3 Statistics of the Main Grid

All models of initial mass $M_{ZAMS} \geq 90 M_{\odot}$ ended with core masses above our limit calculated in Section 3. The exception is at Z_{SMC} where the line is just above the $90 M_{\odot}$ limit. As such, almost our entire model population of BH candidate models arrive from the initial mass range of $M_{ZAMS} = 60 - 80 M_{\odot}$. While the rest of the models undergo PI and therefore do not form part of our BH candidates, they are valuable for examining trends, which factors into the fits of Section 5. Overall, 41 of our 336 models ended their evolution with CO cores below the predicted limit. The division of these parameters are described in the following paragraphs.

At $M_{ZAMS} = 80 M_{\odot}$ there are 13 models which had CO core masses below the PI limit. The majority (9/13 models for this initial mass) of BH candidate models lost less than $10 M_{\odot}$ during their evolution, while a few more (4/13) ended up with final masses between $61 - 70 M_{\odot}$. These low final mass candidates were due to strong winds at Z_{SMC} , with high rotation models losing approx $5 M_{\odot}$ more due to the model's resulting position in temperature space. Models with $M_{ZAMS} = 80 M_{\odot}$ at low metallicity (1/100th Z_{\odot}) were able to successfully remove enough angular momentum to avoid critical rotation. Models at $M_{ZAMS} = 60 M_{\odot}$, had 35 models with CO core masses below the PI limit. Most of these models (21/35) had final masses above $50 M_{\odot}$, while the rest had final masses between $46-60 M_{\odot}$. The models with low masses were primarily contributed

to by metallicities of 1/10 th Z_{\odot} or Z_{SMC} . Especially noticeable is that, at this initial mass, some (12/35) models of high overshooting ($\alpha_{ov} = 0.5$) were able to produce BH candidates in our applicable mass range (nominally, $M_{final} > 50 M_{\odot}$), which is not the case in the case where $M_{ZAMS} = 80 M_{\odot}$.

To conclude this section, we have shown that α_{ov} and M_{ZAMS} are critical parameters for M_{core} , and that Z , M_{ZAMS} , and α_{ov} are critical parameters for M_f , which we will use in the following section to parameterise our fits for the models. Additionally, we have found a metallicity dependent Ω/Ω_{crit} limit. This limit, which can be seen sketched in Figure 7, defines where a model would lose insufficient mass in order to remain below breakup speeds during the evolution. This was not found to be mass dependent in our range of ZAMS masses. This makes low metallicity models more susceptible to extreme mass loss, and thus lowering their potential black hole mass. Finally, we determine that semiconvection is unimportant within our parameter range in determining the final mass of a model, or its susceptibility to PI.

5 NUMERICAL FITS OF M_{CORE} AND M_{FINAL}

Based on our detailed stellar evolution models, we produce fits that may have use for population synthesis by ourselves or others. As established in Section 4, a set of clear relationships exist across the parameter space. Equation 1 gave M_f as a function of core mass M_{core} and envelope mass M_{envl} , which themselves are functions of our parameters. By fitting functions to these parameters, we can create a relation for the final mass.

Firstly, we look at the subset of our parameter space where $\Omega/\Omega_{crit} = 0.2$, and $\alpha_{sc} = 1$, as low rotating models are more likely to be stable and semiconvection is not a dominant variable (as per Section 4). With this, we further define:

$$M_{core} = f(M_{ZAMS}, \alpha_{ov}), \quad (6)$$

$$M_{final} = f(M_{ZAMS}, Z, \alpha_{ov}) \quad (7)$$

By fitting the He core sizes to M_{ZAMS} and α_{ov} based on 21 (7 M_{ZAMS} by 3 α_{ov}) models at constant $Z = 1/10$ th Z_{\odot} , we achieve the following relation:

$$M_{He \text{ core, fit}} = -6.98(\pm 1.6) + 0.51(\pm 0.015) \cdot M_{ZAMS} + 0.35(\pm 0.19)\alpha_{ov} \cdot M_{ZAMS}^{1.03(\pm 0.11)} \quad (8)$$

which has a root mean square error of $0.82 M_{\odot}$. As mentioned, this relation was calculated for a constant metallicity value. However, when taking into account other metallicities, there was not a significant difference in the value of these coefficients, as metallicity does not have a significant effect on the core mass. The limit to this relation is approximately $Z < 1/100$ th Z_{\odot} , for the same reasons described in Section 4.2.

The mass of the convective core during the main sequence, which ultimately decides the mass of the formed Helium or Carbon-Oxygen core, is proportional to the ZAMS mass. In Equation 8, we show that a linear relation well approximates the correlation between the core and ZAMS mass in the mass range considered in this study. This is because the core-to-total mass ratio increases with the ZAMS mass but then plateaus off as one approaches higher and higher ZAMS masses (see Yusof et al. 2013; Sabhahit et al. 2022), which means the core and ZAMS mass relation approaches a linear trend. This might however break down for ZAMS masses beyond the mass

range considered here. The main contributing factor towards such a departure from a linear relation is a switch to an optically thick wind, which is capable of eating away the core mass and significantly reducing it. However we note that such a switch to optically thick wind physics is metallicity dependent as shown in [Sabhahit et al. \(2023\)](#), shifting to higher ZAMS masses towards lower Z . The model grid considered in this study largely avoids the optically-thick wind physics regime due to low Z and the correlation between the core and ZAMS mass holds well.

Through fitting another set of 84 models, varying α_{ov} , M_{ZAMS} and Z for the final mass of the star, M_{final} , we achieve:

$$M_{final, fit} = M_{ZAMS} \left[1(\pm 0.006) - \left(0.02(\pm 0.009) + 0.05(\pm 0.019)\alpha_{ov} \right) \cdot M_{ZAMS}^{0.65 \pm 0.076} \cdot \left(\frac{Z}{Z_{\odot}} \right)^{0.72 \pm 0.057} \right] \quad (9)$$

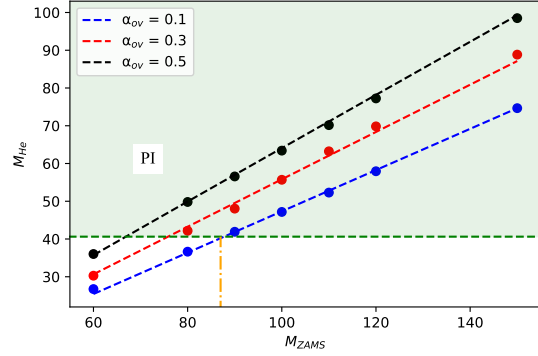
This equation is accurate for $Z_{SMC} < Z < 1/1000$ th Z_{\odot} and has a root mean square error of $3.09 M_{\odot}$. To find any BH mass within our range using our fits, first apply a $40.6 M_{\odot}$ helium core mass limit, as discussed in Section 3 from which we can plot Equation 8 in Figure 9a and map the maximum initial mass before PI (x-axis) to the fits depending on a value of overshooting. It can be seen that, since the line fit trends to the left with increasing overshooting, that increasing overshooting has a negative correlation with the maximum initial mass before PI. We can do a similar mapping with Equation 9, plotted in Figure 9b this time for different values of metallicity.

In the limit of zero overshooting and metallicity, we obtain a maximum black hole mass of $M_{BH} = 93.3 M_{\odot}$ which describes the physical maximum. Table 3 shows no black holes within the $90 - 95 M_{\odot}$ range as the limit of our grid with α_{ov} is 0.1 and Z is $1/1000$ th Z_{\odot} .

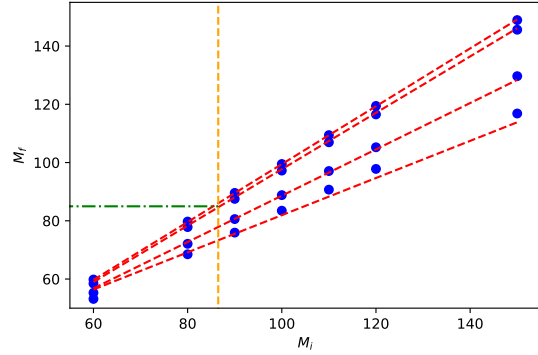
6 POPULATING THE PI GAP

For this section, we populate the traditional PI mass gap ($> 50 M_{\odot}$) informed by the equations in Section 5. A sample of 240,000 stars - 10,000 stars for 3 values of overshooting and 8 metallicities - are populated between initial masses $60 < M_{ZAMS} < 100 M_{\odot}$. Equal distribution on the log scale from Z_{SMC} to $1/1000$ th Z_{\odot} is assumed to obtain the metallicity values. Then we use Equation 8 to evaluate the He core size and check whether the model becomes pair unstable or not. Additionally, Equation 9 is used to inform on the mass of the resulting BH. Tables 2 and 3 provide a detailed breakdown of our BH population, and weighs this against the Salpeter IMF ($M_{-2.35}$) for the population of 240,000 stars considered.

The 240,000 stars are initially divided into mass bins $60 - 70$, $70 - 80$, $80 - 90$, and $90 - 100 M_{\odot}$ and the IMF-weighted fractions are shown in the second column of Table 2. The next three columns show the contributions from individual overshooting values. The final column shows the fraction of black holes formed corresponding to the initial mass range. This column takes into consideration of both the IMF weighting of the stars and the He core mass staying below $40.6 M_{\odot}$ according to Equation 8. In the low mass bin ($M_{ZAMS} = 60 - 70 M_{\odot}$), the three overshooting values contribute almost equally to the BH population, as the cores of these stars are too small regardless of the overshooting values in our range. As the initial mass range increases, we can see that the contribution towards heavy black holes becomes a strong function of overshooting. This is because as the



(a)



(b)

Figure 9. Subfigure 9a includes fitted lines for Helium core masses at constant $\Omega/\Omega_{crit} = 0.2$, metallicity $Z = 1/10$ th Z_{\odot} , and semiconvection $\alpha_{sc} = 1$, from Equation 8. The black, red and blue dots are data values from the models for overshooting values of $\alpha_{ov} = 0.5, 0.3, 0.1$ respectively, while the corresponding dashed lines are the fits for those values, and the green dashed line represents our calculated Helium core PI boundary $M_{He}^{critical} = 40.6 M_{\odot}$. The greenshaded region represents where models would undergo PI. Subfigure 9b fits final masses as a function of initial mass and metallicity, with constant $\alpha_{ov} = 0.1$, $\Omega/\Omega_{crit} = 0.2$, and $\alpha_{sc} = 1$. Using the maximum initial mass in subfigure 9a, which is then marked in subfigure 9b by the orange line, the maximum final mass of the star is then correlated with the green line.

initial mass increases, so does the core size. This strongly disfavours the higher overshooting values as a He core mass of $40.6 M_{\odot}$ is considered our PI condition. In the $85-90 M_{\odot}$ range, only a small fraction of the models can form heavy black holes, while the remaining go pair unstable. This shows that the production of heavy BHs in the PI gap, is not just a product of the IMF, but also of the amount of overshooting (extra mixing), showcased by the last column.

In Table 3, we show the mass distribution of our IMF. All of the stars in this table have a He core mass less than $40.6 M_{\odot}$. The next three columns show the contribution from each overshooting value. A clear gradient is noticeable in the absolute BH numbers as a function of overshooting, which is a direct imprint from the previous table. Very heavy black holes with masses $M_{BH} > 80 M_{\odot}$ are only attainable at low overshooting. The maximum BH mass that can be attained with 0.3 overshooting is below $80 M_{\odot}$. This then forms a gradient of decreasing maximum BH mass as overshooting increases, culminating in a maximum BH mass of $65 - 70 M_{\odot}$ at $\alpha_{ov} = 0.5$.

Additionally, the proportion of black holes also changes drastically

M_{ZAMS}	N_{bin}/N_{Total}	$N_{\alpha_{ov}=0.1}$	$N_{\alpha_{ov}=0.3}$	$N_{\alpha_{ov}=0.5}$	N_{BH}/N_{Total}
60-70	0.38	1/3	1/3	2/7	0.36
70-80	0.27	1/3	1/5	0	0.14
80-90	0.2	1/4	0	0	0.049
90-100	0.15	0	0	0	0

Table 2. Based on a population of 240,000 stars, this table shows the proportion of each initial mass bin (M_{ZAMS}) which forms black holes based on Equation 8. The second column gives the number of stars in that mass bin as a fraction of the entire population - this is entirely based on the IMF. The next set of columns shows the ratio of models which form black holes under different values of overshooting (α_{ov}) for that population. The final column gives the number of black holes for that population as a fraction of the entire population of stars.

M_{BH}	N_{BH}	$N_{BH \alpha_{ov}=0.1}$	$N_{BH \alpha_{ov}=0.3}$	$N_{BH \alpha_{ov}=0.5}$	$N_{BH \text{ SMC-10th}}$	$N_{BH \text{ 10th-100th}}$	$N_{BH \text{ 100th-1000th}}$
60-65	40077	15948	13906	10221	5512	15845	18718
65-70	26137	13420	10918	1799	3782	10383	11973
70-75	16800	10314	6485	0	1970	6224	8606
75-80	8890	8363	526	0	797	3887	4207
80-85	5595	5595	0	0	0	2416	3179
85-90	967	967	0	0	0	0	967
90-95	0	0	0	0	0	0	0

Table 3. This table, using the same data and population of 240,000 stars as the previous (Table 2), bins the masses of the black holes in brackets of $5 M_{\odot}$. The second column gives the total absolute number of black holes for each mass bin. Columns 3-5 separate the effects of overshooting, with each column contributing black holes from one value of α_{ov} . Columns 6-8 split the models up based on metallicity, with each column showing the contribution of a range of metallicities to the total BH population.

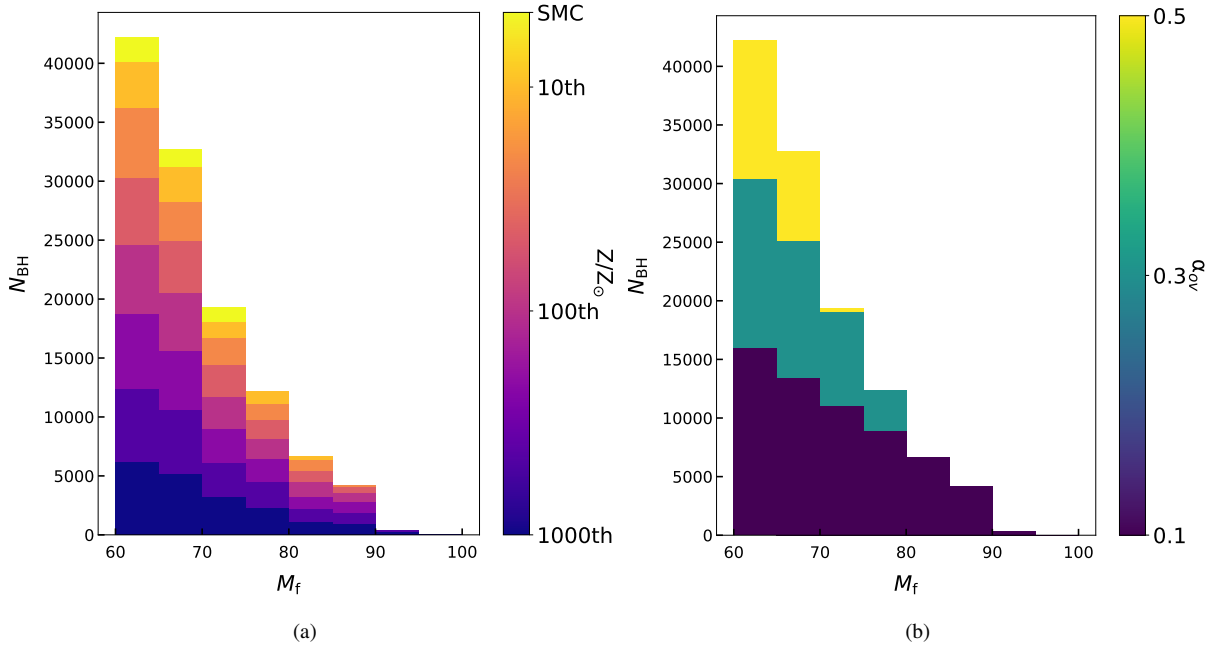


Figure 10. Graphical representation of the numbers plotted in Table 3. Colours are arranged based on logarithmic metallicity in subfigure 10a, and α_{ov} in subfigure 10b. The x-axis represents each mass bin, while the y-axis is the total number of stars in that bin, coloured based on each parameter.

depending on overshooting value, with higher overshooting resulting in fewer numbers of black holes in the same mass bin, as a correlative lower overshooting value. An exception to this is in the lowest mass bracket, where the progenitors have equal distributions across all values of overshooting. This is due to most of these black holes originating from the 60-70 M_{\odot} initial mass range.

The last three columns of Table 3 give the absolute numbers distributed in three metallicity bins. We notice a gradient towards lower metallicities producing higher mass black holes, and in larger quantities. Similarly to high overshooting, the number of black holes drops off for higher mass bins. From our equations, the heaviest black hole

is in the mass range 90 – 95 M_{\odot} and the required conditions are low overshooting ($\alpha_{ov} \leq 0.1$) and low metallicity below 1/100 th Z_{\odot} .

Even though low overshooting and low metallicity are the most likely to produce the heaviest black holes, we can still see that large amounts of mixing can still result in BH production inside of the PI mass gap. This is counter-intuitive for such high overshooting, but encouraging, as it shows that the PI mass gap still *shrinks* - even in the presence of larger amounts of CBM.

Finally, we quantify the ratio of low and high mass black holes within the PI mass gap, in an effort to help inform observations. For this, we will take the total number of black holes, across all

metallicity and mixing values, and include only the values within the $60 - 70 M_{\odot}$ and $80 - 90 M_{\odot}$ brackets, representing the lowest and highest mass black holes. We arrive at an approximate ratio of 10 : 1, rounded to the nearest integer.

7 DISCUSSION

In this paper we have shown that the critical CO (or He) core mass does not depend on stellar modelling inputs such as core overshooting (α_{ov}), initial rotation rate (Ω), or semi-convection (α_{sc}) (see upper panel Figure 3). The final mass (M_{final}) and also the black hole mass (M_{BH}) do however depend on these inputs, but on some (α_{ov}) very strongly, and on others (α_{sc}) hardly at all in this regime. One could ask the question if there are any other parameters that we have not tested that could affect our results. Two notable aspects that have been discussed in recent literature are the $^{12}\text{C}(\alpha,\gamma)^{16}\text{O}$ reaction rate (Farmer et al. 2019; Belczynski 2020; Costa et al. 2021) and envelope undershoot (Costa et al. 2021). We discuss these two aspects in the next few paragraphs.

We first tested the effects of varying the $^{12}\text{C}(\alpha,\gamma)^{16}\text{O}$ reaction rate on the M_{CO} core mass near the PI gap. The thermonuclear reaction rates by Xu et al. (2013) in NACRE II, which are implemented in the MESA code, are temperature-dependent and have upper and lower limits on the reaction for a given temperature range. As the uncertainty on the $^{12}\text{C}(\alpha,\gamma)^{16}\text{O}$ rate is not a simple gaussian, but changes non-linearly with temperature, we test the upper and lower limits of the nuclear reactions as provided by the experimental data in Xu et al. (2013). At an initial ZAMS mass of $90 M_{\odot}$ our stellar models are at the PI limit, and as such we test the upper and lower limits of the $^{12}\text{C}(\alpha,\gamma)^{16}\text{O}$ rate at the critical point. For this initial mass, the central temperature post-Helium burning ranges from 0.4-0.7 (10^9K). We therefore adopt the lower and upper rates from Xu et al. (2013) for this temperature range, which corresponds to a factor of 0.845 for the lower boundary and 1.16 for the upper boundary of the standard reaction rate. Our results show that the M_{CO} changes by at most 1-2 M_{\odot} when adopting the lower or upper rates in this temperature range. Note that we have not systematically run critical M_{CO} experiments, as performed in for instance Farmer et al. (2020) for H-poor models.

We next tested the effect of convective shell undershooting in our stellar models, with comparable $\alpha_{\text{ov}} = 0.1$ during core H-burning and $\alpha_{\text{under}} = 0.1$ on the H-shell during core He-burning, near the PI boundary with $M_{\text{ZAMS}} = 90 M_{\odot}$. We find that the effect on the M_{CO} core is negligible with a difference of only $0.4 M_{\odot}$ when compared to models with no undershooting. However, recent 3D hydrodynamic models (Cristini et al. 2016, 2019; Rizzuti et al. 2023), show that due to the stiffness of the lower boundary of convective shells, which means that the boundary is harder to penetrate, the convective undershoot value is found to be 1/5th of the upper overshoot value. By comparing the bulk Richardson's number in Rizzuti et al. (2022) Table 1, we indeed see that the lower boundary is approximately 1/5th of the upper boundary for all 3D hydrodynamic models. Moreover, by comparing the velocities of the lower and upper convective boundaries in their Figure 3, we see that the velocities are significantly reduced at the lower boundary in comparison to the upper convective boundary, confirming that the convective mixing is reduced substantially below convective shells. See also Cristini et al. (2016, 2019); Rizzuti et al. (2023).

So we have established that Equation 9 may indeed represent an accurate representations of the final masses (M_{final}) of our detailed stellar evolution modelling. However, what we have not yet discussed

if our BH masses are accurately represented. As we mentioned at the start our strategy is to compute M_{final} and on the basis of hydrodynamical calculations of Fernández et al. (2018) we assume this to be linked to the final BH masses. There is one more important aspect of assumptions in our stellar evolution modelling to be discussed and that is how PPI might affect our results. As mentioned earlier, our lower PI boundary is the one between direct BH formation versus the onset of PI. It will only be the models towards the upper edge of the PI gap that will explode as PISNe, while those at lower masses may lose mass pulsationally and still form BHs. Figure 2 in Farmer et al. (2019) is rather illustrative in this context. For models just above the BH/PI boundary it is shown that while PI pulses operate, this hardly affects the final masses. Only when models are comfortably above the BH/PI boundary (by roughly $10 M_{\odot}$) do pulses remove significant amounts of mass that could affect our BH mass distribution (see also Woosley & Heger 2021). We will now estimate how PPI may affect our BH mass distribution.

First, our BH distribution is dominated by ZAMS masses in the range $50-90 M_{\odot}$ while PI (including both PPI and PISNe) is considered to occur between 90 and $130 M_{\odot}$. While we cannot exactly tell the mass boundary between PPI and PISNe, we assume that roughly half the objects in this $90-130 M_{\odot}$ range produce PISNe (thereby not contributing to BH formation) and the other half producing PPI. It is only this $\sim 1/2$ of the $90-130 M_{\odot}$ mass bin that could affect our BH mass distribution. The second relevant realisation is that the IMF dictates that there are ~ 3 times more stars in the mass bin between 50 and $90 M_{\odot}$ than in the $90-130 M_{\odot}$ range. In other words, our BH mass distribution could be affected by about a factor $1/2 \times 1/3 = 1/6$, and is considered to be 83% accurate. Future hydrodynamical PPI modelling is expected to improve our BH mass distribution.

In any case, despite this potential pollution, we can be confident that our BH mass provides meaningful insights into the true BH mass distribution for single stars. And while in the case of BH-BH merger events, binary evolution (Belczynski et al. 2016; Breivik et al. 2016; Kruckow et al. 2018; Marchant et al. 2019; Bavera et al. 2020; Broekgaard et al. 2021) would need to be contemplated, especially if the bulk of BH-BH mergers would arise from the isolated binary scenario, we would expect binary evolution affects to mostly affect the lower range of our BH mass distribution. The upper part of our BH mass distribution, and especially the maximum BH mass, is not expected to depend on such additional complexities. In any case, even if we do not perform binary evolution, and cannot predict GW rates or the overall BH distribution originating from binary evolution, the specific observational BH maximum *feature* in the LIGO/Virgo data (of O4 and beyond) can be tested in a meaningful way against our maximum BH mass from single star evolution. Should the maximum (below PI) BH mass indeed turn out to be close to $93 M_{\odot}$ then this would provide confidence in our understanding of stellar evolution of the most massive stars. Should the maximum BH distribution appear notably different instead, then this would challenge our understanding of stellar evolution. One of the aspects that we would be particularly interested in testing further is that of α_{ov} as this is the parameter that is empirically still highly uncertain, yet we found it to have the largest effect.

Should even the uncertain stellar physics of CBM be resolved, but our predictions would differ from the GW features then this might indicate that the nuclear Astrophysics, and in particular the uncertain $^{12}\text{C}(\alpha,\gamma)^{16}\text{O}$ rate (Takahashi 2018; Farmer et al. 2020; Shen et al. 2020; Farag et al. 2022), should be adapted.

8 CONCLUSIONS

We have systematically investigated the Pair Instability region for very massive stars according to varying parameters of initial mass, overshooting, metallicity, rotation and semiconvection using the MESA stellar evolution code. In doing so, we have mapped out the effect of each of these parameters independently, and in relation to each other. This study also reduced the number of assumptions made about the formation of black holes in this region by considering the full evolution of the stars.

A summary of our conclusions is as follows:

- We find the PI boundary at critical core masses of $M_{\text{CO}}^{\text{critical}} > 36.3 \pm 1.8 M_{\odot}$ for Carbon-Oxygen $M_{\text{He}}^{\text{critical}} > 40.6 \pm 1.5 M_{\odot}$ for Helium.
- The absolute maximum ZAMS mass for a first-generation BH in the PI boundary is $\approx 93.3 M_{\odot}$, which would also be the maximum BH mass in the physical limit.
- While the upper limit of final mass is very strict in terms of appropriate parameters, stars of lower final mass are able to have higher values of rotation or overshooting. However rotation and overshooting remain the dominant parameters in limiting the maximum initial mass for BHs.
- We have analytically fit the core mass and final mass of the star to a pair of equations (Equations 8 and 9) which, together, provide a picture of the entire massive BH parameter space.
- As per our equations, overshooting is the dominant parameter for determining core size, aside from initial mass. Metallicity is the dominant parameter for determining envelope mass, and thus also prospective BH mass.
- Rotation is also an important parameter, and is the only parameter which has a large effect with regards to both core mass and envelope mass. Additionally, rotation is able to influence the potential for a model to undergo supercritical mass loss, however this is also dependent on metallicity. Thus, high rotation ($\Omega/\Omega_{\text{crit}} > 0.4$) could stop BH production at low metallicity ($Z < 1/100$ th Z_{\odot}).
- Contrary to the case of lower mass blue supergiants (Langer & Maeder 1995; Schootemeijer et al. 2019; Higgins & Vink 2020), semiconvection is seen to be unimportant at our very high mass range, as it is completely overshadowed by overshooting and rotation.
- Lastly, we produce a population of BH candidates using our aforementioned equations to inform the distribution of stars. From this, we estimate that the ratio of producing a BH in the lower boundary of the mass gap ($60-70 M_{\odot}$) compared to the maximum ($80-90 M_{\odot}$) is approximately 10 : 1.

ACKNOWLEDGEMENTS

The authors acknowledge MESA authors and developers for their continued revisions and public accessibility of the code. EW is funded by ST/W507925/1. JSV and ERH are supported by STFC funding under grant number ST/V000233/1. The authors would also like to thank the anonymous referee for their constructive comments which helped improve the presentation of the results.

DATA AVAILABILITY

Input files for variables will be made publicly accessible via the MESA marketplace.

REFERENCES

- Abbott B. P., et al., 2016, *Phys. Rev. Lett.*, **116**, 061102
- Abbott R., et al., 2020, *Phys. Rev. Lett.*, **125**, 101102
- Abbott R., et al., 2023, *Physical Review X*, **13**, 011048
- Aerts C., Mathis S., Rogers T. M., 2019, *ARA&A*, **57**, 35
- Anders E. H., Pedersen M. G., 2023, *Galaxies*, **11**, 56
- Barkat Z., Rakavy G., Sack N., 1967, *Phys. Rev. Lett.*, **18**, 379
- Bavera S. S., et al., 2020, *A&A*, **635**, A97
- Belczynski K., 2020, *ApJ*, **905**, L15
- Belczynski K., Bulik T., Fryer C. L., Ruiter A., Valsecchi F., Vink J. S., Hurley J. R., 2010, *ApJ*, **714**, 1217
- Belczynski K., Holz D. E., Bulik T., O’Shaughnessy R., 2016, *Nature*, **534**, 512
- Björklund R., Sundqvist J. O., Puls J., Najarro F., 2021, *A&A*, **648**, A36
- Bond J. R., Arnett W. D., Carr B. J., 1984, *ApJ*, **280**, 825
- Bowman D. M., 2020, *Frontiers in Astronomy and Space Sciences*, **7**, 70
- Breivik K., Rodriguez C. L., Larson S. L., Kalogera V., Rasio F. A., 2016, *ApJ*, **830**, L18
- Bressan A., Marigo P., Girardi L., Salasnich B., Dal Cero C., Rubele S., Nanni A., 2012, *MNRAS*, **427**, 127
- Briquet M., Morel T., Thoul A., Scuflaire R., Miglio A., Montalbán J., Dupret M. A., Aerts C., 2007, *MNRAS*, **381**, 1482
- Broekgaarden F. S., et al., 2021, *MNRAS*, **508**, 5028
- Casares J., Jonker P. G., 2014, *Space Sci. Rev.*, **183**, 223
- Choi J., Dotter A., Conroy C., Cantiello M., Paxton B., Johnson B. D., 2016, *ApJ*, **823**, 102
- Claret A., Torres G., 2016, *A&A*, **592**, A15
- Claret A., Torres G., 2017, *ApJ*, **849**, 18
- Constantino T., Baraffe I., 2018, *A&A*, **618**, A177
- Costa G., Girardi L., Bressan A., Marigo P., Rodrigues T. S., Chen Y., Lanza A., Goudfrooij P., 2019, *MNRAS*, **485**, 4641
- Costa G., Bressan A., Mapelli M., Marigo P., Iorio G., Spera M., 2021, *MNRAS*, **501**, 4514
- Costa G., Ballone A., Mapelli M., Bressan A., 2022, *MNRAS*, **516**, 1072
- Cox J. P., Giuli R. T., 1968, Principles of stellar structure
- Cristini A., Meakin C., Hirschi R., Arnett D., Georgy C., Viallet M., 2016, *Phys. Scr.*, **91**, 034006
- Cristini A., Hirschi R., Meakin C., Arnett D., Georgy C., Walkington I., 2019, *MNRAS*, **484**, 4645
- Di Carlo U. N., Giacobbo N., Mapelli M., Pasquato M., Spera M., Wang L., Haardt F., 2019, *MNRAS*, **487**, 2947
- Dupret M. A., Thoul A., Scuflaire R., Daszyńska-Daszkiewicz J., Aerts C., Bourge P. O., Waelkens C., Noels A., 2004, *A&A*, **415**, 251
- Eggenberger P., Meynet G., Maeder A., Hirschi R., Charbonnel C., Talon S., Ekström S., 2008, *Ap&SS*, **316**, 43
- Ekström S., et al., 2012, *A&A*, **537**, A146
- Farag E., Renzo M., Farmer R., Chidester M. T., Timmes F. X., 2022, *ApJ*, **937**, 112
- Farmer R., Renzo M., de Mink S. E., Marchant P., Justham S., 2019, *ApJ*, **887**, 53
- Farmer R., Renzo M., de Mink S. E., Fishbach M., Justham S., 2020, *ApJ*, **902**, L36
- Fernández R., Quataert E., Kashiyama K., Coughlin E. R., 2018, *MNRAS*, **476**, 2366
- Fishbach M., Holz D. E., 2020, *ApJ*, **904**, L26
- Fowler W. A., Hoyle F., 1964, *ApJS*, **9**, 201
- Fragione G., Loeb A., Rasio F. A., 2020, arXiv e-prints, p. arXiv:2009.05065
- Gal-Yam A., et al., 2009, *Nature*, **462**, 624
- Gilkis A., Shenar T., Ramachandran V., Jermyn A. S., Mahy L., Oskinova L. M., Arcavi I., Sana H., 2021, *MNRAS*, **503**, 1884
- Gräfener G., Owocki S. P., Vink J. S., 2012, *A&A*, **538**, A40
- Grassitelli L., Langer N., Mackey J., Gräfener G., Grin N. J., Sander A. A. C., Vink J. S., 2021, *A&A*, **647**, A99
- Grevesse N., Sauval A. J., 1998, *Space Sci. Rev.*, **85**, 161
- Heger A., Langer N., Woosley S. E., 2000, *ApJ*, **528**, 368
- Heger A., Fryer C. L., Woosley S. E., Langer N., Hartmann D. H., 2003, *ApJ*, **591**, 288

- Higgins E. R., Vink J. S., 2019, *A&A*, **622**, A50
- Higgins E. R., Vink J. S., 2020, *A&A*, **635**, A175
- Higgins E. R., Vink J. S., 2023, *MNRAS*, **518**, 1158
- Higgins E. R., Sander A. A. C., Vink J. S., Hirschi R., 2021, *MNRAS*, **505**, 4874
- Ishii M., Ueno M., Kato M., 1999, *PASJ*, **51**, 417
- Jiang Y.-F., Cantiello M., Bildsten L., Quataert E., Blaes O., 2015, *ApJ*, **813**, 74
- Kalari V. M., Vink J. S., Dufton P. L., Fraser M., 2018, *A&A*, **618**, A17
- Kato S., 1966, *PASJ*, **18**, 374
- Kimball C., et al., 2021, *ApJ*, **915**, L35
- Klencki J., Nelemans G., Istrate A. G., Chruslinska M., 2021, *A&A*, **645**, A54
- Köhler K., et al., 2015, *A&A*, **573**, A71
- Krtićka J., Kubát J., 2017, *A&A*, **606**, A31
- Kruckow M. U., Tauris T. M., Langer N., Kramer M., Izzard R. G., 2018, *MNRAS*, **481**, 1908
- Lam C. Y., et al., 2022, *ApJ*, **933**, L23
- Langer N., 1998, *A&A*, **329**, 551
- Langer N., 2012, *ARA&A*, **50**, 107
- Langer N., Maeder A., 1995, *A&A*, **295**, 685
- Langer N., El Eid M. F., Fricke K. J., 1985, *A&A*, **145**, 179
- Limongi M., Chieffi A., 2018, *ApJS*, **237**, 13
- Maeder A., Meynet G., 2000a, *ARA&A*, **38**, 143
- Maeder A., Meynet G., 2000b, *A&A*, **361**, 159
- Maeder A., Zahn J.-P., 1998, *A&A*, **334**, 1000
- Marchant P., Moriya T. J., 2020, *A&A*, **640**, L18
- Marchant P., Renzo M., Farmer R., Pappas K. M. W., Taam R. E., de Mink S. E., Kalogera V., 2019, *ApJ*, **882**, 36
- Meynet G., Ekström S., Maeder A., 2006, in , *Chemical Abundances and Mixing in Stars in the Milky Way and its Satellites*. p. 314, doi:10.1007/978-3-540-34136-9_100
- Müller P. E., Vink J. S., 2014, *A&A*, **564**, A57
- Nugis T., Lamers H. J. G. L. M., 2000, *A&A*, **360**, 227
- Orosz J. A., McClintock J. E., Aufdenberg J. P., Remillard R. A., Reid M. J., Narayan R., Gou L., 2011, *ApJ*, **742**, 84
- Paxton B., Bildsten L., Dotter A., Herwig F., Lesaffre P., Timmes F., 2011, *ApJS*, **192**, 3
- Paxton B., et al., 2013, *ApJS*, **208**, 4
- Paxton B., et al., 2015, *ApJS*, **220**, 15
- Paxton B., et al., 2018, *ApJS*, **234**, 34
- Paxton B., et al., 2019, *ApJS*, **243**, 10
- Petrovic J., Pols O., Langer N., 2006, *A&A*, **450**, 219
- Ramachandran V., et al., 2019, *A&A*, **625**, A104
- Ramírez-Agudelo O. H., et al., 2013, *A&A*, **560**, A29
- Ramírez-Agudelo O. H., et al., 2017, *A&A*, **600**, A81
- Renzo M., Farmer R. J., Justham S., de Mink S. E., Göteborg Y., Marchant P., 2020a, *MNRAS*, **493**, 4333
- Renzo M., Cantiello M., Metzger B. D., Jiang Y. F., 2020b, *ApJ*, **904**, L13
- Rizzuti F., Hirschi R., Georgy C., Arnett W. D., Meakin C., Murphy A. S., 2022, *MNRAS*, **515**, 4013
- Rizzuti F., Hirschi R., Arnett W. D., Georgy C., Meakin C., Murphy A. S., Rauscher T., Varma V., 2023, *MNRAS*, **523**, 2317
- Rogers F. J., Nayfonov A., 2002, *ApJ*, **576**, 1064
- Romagnolo A., Belczynski K., Klencki J., Agrawal P., Shenar T., Szécsi D., 2022, *arXiv e-prints*, p. arXiv:2211.15800
- Romero-Shaw I. M., Lasky P. D., Thrane E., Calderon Bustillo J., 2020, *arXiv e-prints*, p. arXiv:2009.04771
- Sabhahit G. N., Vink J. S., Higgins E. R., Sander A. A. C., 2021, *MNRAS*, **506**, 4473
- Sabhahit G. N., Vink J. S., Higgins E. R., Sander A. A. C., 2022, *MNRAS*, **514**, 3736
- Sabhahit G. N., Vink J. S., Sander A. A. C., Higgins E. R., 2023, *MNRAS*, **524**, 1529
- Sabín-Sanjulián C., et al., 2017, *A&A*, **601**, A79
- Sander A. A. C., Vink J. S., 2020, *MNRAS*, **499**, 873
- Schootemeijer A., Langer N., Grin N. J., Wang C., 2019, *A&A*, **625**, A132
- Schulze S., et al., 2023, *arXiv e-prints*, p. arXiv:2305.05796
- Scott L. J. A., Hirschi R., Georgy C., Arnett W. D., Meakin C., Kaiser E. A., Ekström S., Yusof N., 2021, *MNRAS*, **503**, 4208
- Shen Y. P., et al., 2020, *Phys. Rev. Lett.*, **124**, 162701
- Spera M., Mapelli M., Bressan A., 2015, *MNRAS*, **451**, 4086
- Spera M., Mapelli M., Giacobbo N., Trani A. A., Bressan A., Costa G., 2019, *MNRAS*, **485**, 889
- Stothers R. B., 1999, *MNRAS*, **305**, 365
- Szécsi D., Langer N., Yoon S.-C., Sanyal D., de Mink S., Evans C. J., Dermine T., 2015, *A&A*, **581**, A15
- Takahashi K., 2018, *ApJ*, **863**, 153
- Tanikawa A., Susa H., Yoshida T., Trani A. A., Kinugawa T., 2021, *ApJ*, **910**, 30
- Vink J. S., 2022, *ARA&A*, **60**, 203
- Vink J. S., Gräfener G., 2012, *ApJ*, **751**, L34
- Vink J. S., de Koter A., 2005, *A&A*, **442**, 587
- Vink J. S., de Koter A., Lamers H. J. G. L. M., 2001, *A&A*, **369**, 574
- Vink J. S., Brott I., Gräfener G., Langer N., de Koter A., Lennon D. J., 2010, *A&A*, **512**, L7
- Vink J. S., Muijres L. E., Anthonisse B., de Koter A., Gräfener G., Langer N., 2011, *A&A*, **531**, A132
- Vink J. S., Higgins E. R., Sander A. A. C., Sabhahit G. N., 2021, *MNRAS*, **504**, 146
- Volpato G., Marigo P., Costa G., Bressan A., Trabucchi M., Girardi L., 2023, *ApJ*, **944**, 40
- Wang Y.-Z., Li Y.-J., Vink J. S., Fan Y.-Z., Tang S.-P., Qin Y., Wei D.-M., 2022, *ApJ*, **941**, L39
- Woosley S. E., 2017, *ApJ*, **836**, 244
- Woosley S. E., Heger A., 2021, *ApJ*, **912**, L31
- Woosley S. E., Heger A., Weaver T. A., 2002, *Reviews of Modern Physics*, **74**, 1015
- Xu Y., Takahashi K., Goriely S., Arnould M., Ohta M., Utsunomiya H., 2013, *Nuclear Phys. A*, **918**, 61
- Yoon S. C., Langer N., 2005, *A&A*, **443**, 643
- Yusof N., et al., 2013, *MNRAS*, **433**, 1114
- de Jager C., Nieuwenhuijzen H., van der Hucht K. A., 1988, *A&AS*, **72**, 259

APPENDIX A: TABLE OF MODELS

Summary of all models run as part of the main grid. The first 5 columns describe the parameters of the models, while the 6th and 7th columns give the TAMS mass and Helium core mass. The last three columns provide the final mass, CO core and Helium core masses. Models which did not reach core helium exhaustion did not generate a CO core, and so their M_{CO} core property is left with a dash. Models that likewise did not reach TAMS due to supercritical rotation also have their TAMS column properties (M_{TAMS} , M_{He}) replaced by a dash.

Z	M_{f}	α_{ov}	$\Omega/\Omega_{\text{crit}}$	α_{sc}	M_{TAMS}	M_{He}	M_{f}	M_{CO}	M_{He}
10^{-3}	60	0.1	0.2	1	59	27	59	23	27
10^{-3}	60	0.1	0.2	100	59	27	59	23	28
10^{-3}	60	0.1	0.4	1	59	53	59	-	53
10^{-3}	60	0.1	0.4	100	59	53	59	-	53
10^{-3}	60	0.3	0.2	1	59	29	59	27	30
10^{-3}	60	0.3	0.2	100	59	29	59	-	14
10^{-3}	60	0.3	0.4	1	59	55	59	-	55
10^{-3}	60	0.3	0.4	100	59	55	59	-	55
10^{-3}	60	0.5	0.2	1	59	33	59	31	34
10^{-3}	60	0.5	0.2	100	59	33	59	30	33
10^{-3}	60	0.5	0.4	1	59	56	59	-	56
10^{-3}	60	0.5	0.4	100	59	56	59	-	56
10^{-2}	60	0.1	0.2	1	59	26	58	24	28
10^{-2}	60	0.1	0.2	100	59	30	58	29	33
10^{-2}	60	0.1	0.4	1	59	53	59	-	53
10^{-2}	60	0.1	0.4	100	59	53	59	-	53
10^{-2}	60	0.3	0.2	1	59	29	58	26	30
10^{-2}	60	0.3	0.2	100	59	30	58	25	28
10^{-2}	60	0.3	0.4	1	59	55	59	-	55
10^{-2}	60	0.3	0.4	100	59	55	59	-	55
10^{-2}	60	0.5	0.2	1	59	33	58	32	35
10^{-2}	60	0.5	0.2	100	59	33	58	32	35
10^{-2}	60	0.5	0.4	1	59	56	59	-	56
10^{-2}	60	0.5	0.4	100	59	56	59	-	56
10^{-1}	60	0.1	0.2	1	56	24	55	23	26
10^{-1}	60	0.1	0.2	100	56	26	55	23	27
10^{-1}	60	0.1	0.4	1	54	31	49	31	35
10^{-1}	60	0.1	0.4	100	54	31	47	31	35
10^{-1}	60	0.3	0.2	1	56	28	55	26	30
10^{-1}	60	0.3	0.2	100	56	28	55	25	29
10^{-1}	60	0.3	0.4	1	54	34	47	33	37
10^{-1}	60	0.3	0.4	100	54	34	48	33	37
10^{-1}	60	0.5	0.2	1	54	33	52	32	36
10^{-1}	60	0.5	0.2	100	54	33	52	32	36
10^{-1}	60	0.5	0.4	1	54	39	48	38	42
10^{-1}	60	0.5	0.4	100	54	39	48	38	42
SMC	60	0.1	0.2	1	54	23	53	21	25
SMC	60	0.1	0.2	100	55	23	53	21	24
SMC	60	0.1	0.4	1	52	27	48	26	30
SMC	60	0.1	0.4	100	52	27	49	26	30
SMC	60	0.3	0.2	1	53	28	50	28	31
SMC	60	0.3	0.2	100	53	28	51	26	30
SMC	60	0.3	0.4	1	51	31	48	30	34
SMC	60	0.3	0.4	100	51	31	47	30	34
SMC	60	0.5	0.2	1	51	33	48	32	35
SMC	60	0.5	0.2	100	51	33	48	32	35
SMC	60	0.5	0.4	1	50	35	46	35	38
SMC	60	0.5	0.4	100	50	35	45	35	39
10^{-3}	80	0.1	0.2	1	79	38	79	33	38
10^{-3}	80	0.1	0.2	100	79	38	79	45	51

Z	M_i	α_{ov}	$\Omega/\Omega_{\text{crit}}$	α_{sc}	M_{TAMS}	M_{He}	M_f	M_{CO}	M_{He}
10^{-3}	80	0.1	0.4	1	-	-	79	-	72
10^{-3}	80	0.1	0.4	100	-	-	79	-	72
10^{-3}	80	0.3	0.2	1	79	41	79	36	39
10^{-3}	80	0.3	0.2	100	79	49	79	47	51
10^{-3}	80	0.3	0.4	1	-	-	79	-	74
10^{-3}	80	0.3	0.4	100	-	-	79	-	74
10^{-3}	80	0.5	0.2	1	79	47	79	45	49
10^{-3}	80	0.5	0.2	100	79	47	79	45	48
10^{-3}	80	0.5	0.4	1	79	75	79	-	75
10^{-3}	80	0.5	0.4	100	79	75	79	-	75
10^{-2}	80	0.1	0.2	1	78	37	77	34	39
10^{-2}	80	0.1	0.2	100	78	43	77	41	46
10^{-2}	80	0.1	0.4	1	78	72	78	-	72
10^{-2}	80	0.1	0.4	100	78	72	78	-	72
10^{-2}	80	0.3	0.2	1	78	42	77	37	41
10^{-2}	80	0.3	0.2	100	78	41	77	37	41
10^{-2}	80	0.3	0.4	1	78	74	78	-	74
10^{-2}	80	0.3	0.4	100	78	74	78	-	74
10^{-2}	80	0.5	0.2	1	78	47	77	45	49
10^{-2}	80	0.5	0.2	100	78	47	77	45	49
10^{-2}	80	0.5	0.4	1	78	75	78	-	75
10^{-2}	80	0.5	0.4	100	78	75	78	-	75
10^{-1}	80	0.1	0.2	1	74	35	72	32	36
10^{-1}	80	0.1	0.2	100	74	36	71	33	37
10^{-1}	80	0.1	0.4	1	71	42	66	41	46
10^{-1}	80	0.1	0.4	100	71	42	65	41	46
10^{-1}	80	0.3	0.2	1	73	41	70	37	42
10^{-1}	80	0.3	0.2	100	73	41	70	36	40
10^{-1}	80	0.3	0.4	1	71	46	61	44	49
10^{-1}	80	0.3	0.4	100	71	46	62	43	48
10^{-1}	80	0.5	0.2	1	71	47	67	45	49
10^{-1}	80	0.5	0.2	100	71	47	67	45	49
10^{-1}	80	0.5	0.4	1	71	55	62	53	58
10^{-1}	80	0.5	0.4	100	71	55	64	53	58
SMC	80	0.1	0.2	1	71	33	68	31	35
SMC	80	0.1	0.2	100	71	33	68	30	34
SMC	80	0.1	0.4	1	67	38	63	37	41
SMC	80	0.1	0.4	100	67	38	62	36	41
SMC	80	0.3	0.2	1	67	40	63	40	43
SMC	80	0.3	0.2	100	67	40	63	39	43
SMC	80	0.3	0.4	1	67	43	61	42	46
SMC	80	0.3	0.4	100	67	43	61	40	45
SMC	80	0.5	0.2	1	63	46	57	45	48
SMC	80	0.5	0.2	100	63	46	56	45	48
SMC	80	0.5	0.4	1	64	50	56	49	53
SMC	80	0.5	0.4	100	64	50	57	49	53
10^{-3}	90	0.1	0.2	1	89	43	89	39	45
10^{-3}	90	0.1	0.2	100	89	46	89	42	48
10^{-3}	90	0.1	0.4	1	89	81	89	-	81
10^{-3}	90	0.1	0.4	100	89	81	89	-	81
10^{-3}	90	0.3	0.2	1	89	47	89	40	40
10^{-3}	90	0.3	0.2	100	89	48	89	41	41
10^{-3}	90	0.3	0.4	1	-	-	89	-	84
10^{-3}	90	0.3	0.4	100	-	-	89	-	84
10^{-3}	90	0.5	0.2	1	89	54	89	52	56
10^{-3}	90	0.5	0.2	100	89	54	89	46	46
10^{-3}	90	0.5	0.4	1	89	85	89	-	85

Z	M_i	α_{ov}	$\Omega/\Omega_{\text{crit}}$	α_{sc}	M_{TAMS}	M_{He}	M_{f}	M_{CO}	M_{He}
10^{-3}	90	0.5	0.4	100	89	85	89	-	85
10^{-2}	90	0.1	0.2	1	88	43	87	39	45
10^{-2}	90	0.1	0.2	100	88	46	87	41	47
10^{-2}	90	0.1	0.4	1	88	80	88	-	80
10^{-2}	90	0.1	0.4	100	88	80	88	-	80
10^{-2}	90	0.3	0.2	1	88	47	87	43	48
10^{-2}	90	0.3	0.2	100	88	48	87	41	44
10^{-2}	90	0.3	0.4	1	88	83	88	-	83
10^{-2}	90	0.3	0.4	100	88	83	88	-	83
10^{-2}	90	0.5	0.2	1	88	54	87	51	55
10^{-2}	90	0.5	0.2	100	88	54	87	52	56
10^{-2}	90	0.5	0.4	1	88	85	88	-	85
10^{-2}	90	0.5	0.4	100	88	85	88	-	85
10^{-1}	90	0.1	0.2	1	82	40	80	36	41
10^{-1}	90	0.1	0.2	100	82	42	80	38	43
10^{-1}	90	0.1	0.4	1	80	48	73	47	53
10^{-1}	90	0.1	0.4	100	80	50	70	48	53
10^{-1}	90	0.3	0.2	1	81	47	78	43	48
10^{-1}	90	0.3	0.2	100	81	47	78	43	47
10^{-1}	90	0.3	0.4	1	79	53	69	51	56
10^{-1}	90	0.3	0.4	100	79	53	70	50	56
10^{-1}	90	0.5	0.2	1	79	54	75	52	56
10^{-1}	90	0.5	0.2	100	79	54	75	52	56
10^{-1}	90	0.5	0.4	1	79	62	69	60	65
10^{-1}	90	0.5	0.4	100	79	62	69	60	65
SMC	90	0.1	0.2	1	79	38	75	36	40
SMC	90	0.1	0.2	100	79	39	75	35	39
SMC	90	0.1	0.4	1	75	43	70	41	47
SMC	90	0.1	0.4	100	75	43	69	41	46
SMC	90	0.3	0.2	1	74	46	69	45	50
SMC	90	0.3	0.2	100	74	46	69	45	49
SMC	90	0.3	0.4	1	74	49	68	48	52
SMC	90	0.3	0.4	100	74	49	66	46	51
SMC	90	0.5	0.2	1	68	52	58	51	56
SMC	90	0.5	0.2	100	67	52	59	51	56
SMC	90	0.5	0.4	1	72	57	64	56	60
SMC	90	0.5	0.4	100	72	57	64	56	60
10^{-3}	100	0.1	0.2	1	99	50	99	45	51
10^{-3}	100	0.1	0.2	100	99	51	99	44	50
10^{-3}	100	0.1	0.4	1	-	-	99	-	90
10^{-3}	100	0.1	0.4	100	-	-	99	-	90
10^{-3}	100	0.3	0.2	1	99	55	99	45	45
10^{-3}	100	0.3	0.2	100	99	54	99	43	43
10^{-3}	100	0.3	0.4	1	-	-	99	-	93
10^{-3}	100	0.3	0.4	100	-	-	99	-	93
10^{-3}	100	0.5	0.2	1	99	59	99	55	57
10^{-3}	100	0.5	0.2	100	99	61	99	58	63
10^{-3}	100	0.5	0.4	1	-	-	99	-	95
10^{-3}	100	0.5	0.4	100	-	-	99	-	95
10^{-2}	100	0.1	0.2	1	98	49	97	44	50
10^{-2}	100	0.1	0.2	100	98	53	97	47	54
10^{-2}	100	0.1	0.4	1	98	89	98	-	89
10^{-2}	100	0.1	0.4	100	98	89	98	-	89
10^{-2}	100	0.3	0.2	1	98	54	96	45	51
10^{-2}	100	0.3	0.2	100	98	55	97	45	45
10^{-2}	100	0.3	0.4	1	98	92	98	-	92

Z	M_i	α_{ov}	Ω/Ω_{crit}	α_{sc}	M_{TAMS}	M_{He}	M_f	M_{CO}	M_{He}
10^{-2}	100	0.3	0.4	100	98	92	98	-	92
10^{-2}	100	0.5	0.2	1	97	61	96	59	63
10^{-2}	100	0.5	0.2	100	97	61	96	59	64
10^{-2}	100	0.5	0.4	1	98	94	98	-	94
10^{-1}	100	0.1	0.2	1	91	45	88	41	47
10^{-1}	100	0.1	0.2	100	91	49	88	44	50
10^{-1}	100	0.1	0.4	1	88	54	81	52	58
10^{-1}	100	0.1	0.4	100	88	54	80	51	57
10^{-1}	100	0.3	0.2	1	89	53	86	51	55
10^{-1}	100	0.3	0.2	100	89	53	86	51	55
10^{-1}	100	0.3	0.4	1	88	60	77	57	63
10^{-1}	100	0.3	0.4	100	88	60	78	57	63
10^{-1}	100	0.5	0.2	1	87	60	82	58	63
10^{-1}	100	0.5	0.2	100	87	60	82	58	63
10^{-1}	100	0.5	0.4	1	87	69	77	67	72
10^{-1}	100	0.5	0.4	100	87	69	77	67	72
SMC	100	0.1	0.2	1	87	44	83	40	46
SMC	100	0.1	0.2	100	87	44	83	39	45
SMC	100	0.1	0.4	1	83	49	76	46	52
SMC	100	0.1	0.4	100	83	49	76	46	52
SMC	100	0.3	0.2	1	81	52	75	51	56
SMC	100	0.3	0.2	100	81	52	75	51	55
SMC	100	0.3	0.4	1	82	55	74	54	59
SMC	100	0.3	0.4	100	82	55	72	52	58
SMC	100	0.5	0.2	1	75	59	66	58	62
SMC	100	0.5	0.2	100	76	59	66	57	62
SMC	100	0.5	0.4	1	79	64	71	62	67
SMC	100	0.5	0.4	100	79	64	71	62	67
10^{-3}	110	0.1	0.2	1	109	55	109	49	56
10^{-3}	110	0.1	0.2	100	109	56	109	52	59
10^{-3}	110	0.1	0.4	1	-	-	109	-	99
10^{-3}	110	0.1	0.4	100	-	-	109	-	99
10^{-3}	110	0.3	0.2	1	109	60	109	56	61
10^{-3}	110	0.3	0.2	100	109	60	109	50	50
10^{-3}	110	0.3	0.4	1	-	-	109	-	102
10^{-3}	110	0.3	0.4	100	-	-	109	-	102
10^{-3}	110	0.5	0.2	1	109	66	109	53	53
10^{-3}	110	0.5	0.2	100	109	68	109	64	69
10^{-3}	110	0.5	0.4	1	-	-	109	-	104
10^{-3}	110	0.5	0.4	100	-	-	109	-	104
10^{-2}	110	0.1	0.2	1	107	55	106	49	56
10^{-2}	110	0.1	0.2	100	107	57	107	52	58
10^{-2}	110	0.1	0.4	1	108	96	108	-	96
10^{-2}	110	0.1	0.4	100	108	96	108	-	96
10^{-2}	110	0.3	0.2	1	107	62	106	48	48
10^{-2}	110	0.3	0.2	100	108	61	107	50	50
10^{-2}	110	0.3	0.4	1	108	101	108	-	101
10^{-2}	110	0.3	0.4	100	108	101	108	-	101
10^{-2}	110	0.5	0.2	1	107	67	106	64	68
10^{-2}	110	0.5	0.2	100	107	68	106	64	69
10^{-2}	110	0.5	0.4	1	108	104	108	-	103
10^{-2}	110	0.5	0.4	100	108	104	108	-	103
10^{-1}	110	0.1	0.2	1	100	51	97	46	52
10^{-1}	110	0.1	0.2	100	100	53	96	48	54

Z	M_i	α_{ov}	$\Omega/\Omega_{\text{crit}}$	α_{sc}	M_{TAMS}	M_{He}	M_{f}	M_{CO}	M_{He}
10^{-1}	110	0.1	0.4	1	97	60	89	58	64
10^{-1}	110	0.1	0.4	100	97	61	88	57	64
10^{-1}	110	0.3	0.2	1	97	60	93	58	63
10^{-1}	110	0.3	0.2	100	97	60	93	58	62
10^{-1}	110	0.3	0.4	1	96	67	85	63	69
10^{-1}	110	0.3	0.4	100	96	67	87	63	69
10^{-1}	110	0.5	0.2	1	94	67	89	65	70
10^{-1}	110	0.5	0.2	100	94	67	89	65	70
10^{-1}	110	0.5	0.4	1	95	76	84	73	79
10^{-1}	110	0.5	0.4	100	95	76	84	73	79
SMC	110	0.1	0.2	1	95	49	90	46	51
SMC	110	0.1	0.2	100	95	49	90	45	50
SMC	110	0.1	0.4	1	90	54	83	52	58
SMC	110	0.1	0.4	100	90	54	80	50	57
SMC	110	0.3	0.2	1	86	58	79	57	62
SMC	110	0.3	0.2	100	87	58	79	57	62
SMC	110	0.3	0.4	1	89	62	78	60	65
SMC	110	0.3	0.4	100	89	62	76	59	64
SMC	110	0.5	0.2	1	83	66	73	64	69
SMC	110	0.5	0.2	100	83	66	73	64	69
SMC	110	0.5	0.4	1	86	71	78	69	74
SMC	110	0.5	0.4	100	86	71	78	69	74
10^{-3}	120	0.1	0.2	1	119	60	119	54	60
10^{-3}	120	0.1	0.2	100	119	68	119	65	71
10^{-3}	120	0.1	0.4	1	-	-	119	-	103
10^{-3}	120	0.1	0.4	100	-	-	119	-	105
10^{-3}	120	0.3	0.2	1	119	65	119	58	64
10^{-3}	120	0.3	0.2	100	119	65	119	54	58
10^{-3}	120	0.3	0.4	1	-	-	119	-	111
10^{-3}	120	0.3	0.4	100	-	-	119	-	111
10^{-3}	120	0.5	0.2	1	119	75	119	71	77
10^{-3}	120	0.5	0.2	100	119	75	119	71	77
10^{-3}	120	0.5	0.4	1	-	-	119	-	114
10^{-3}	120	0.5	0.4	100	-	-	119	-	114
10^{-2}	120	0.1	0.2	1	117	61	116	55	61
10^{-2}	120	0.1	0.2	100	117	68	116	63	70
10^{-2}	120	0.1	0.4	1	118	105	118	-	105
10^{-2}	120	0.1	0.4	100	118	95	118	-	100
10^{-2}	120	0.3	0.2	1	117	66	116	60	64
10^{-2}	120	0.3	0.2	100	117	66	114	78	84
10^{-2}	120	0.3	0.4	1	118	110	118	-	110
10^{-2}	120	0.3	0.4	100	118	110	118	-	110
10^{-2}	120	0.5	0.2	1	117	75	116	71	76
10^{-2}	120	0.5	0.2	100	117	75	115	72	77
10^{-2}	120	0.5	0.4	1	118	113	118	-	113
10^{-2}	120	0.5	0.4	100	118	113	118	-	113
10^{-1}	120	0.1	0.2	1	108	56	105	51	57
10^{-1}	120	0.1	0.2	100	108	57	105	52	58
10^{-1}	120	0.1	0.4	1	106	65	98	61	68
10^{-1}	120	0.1	0.4	100	105	68	95	65	72
10^{-1}	120	0.3	0.2	1	105	66	101	64	69
10^{-1}	120	0.3	0.2	100	105	66	101	64	69
10^{-1}	120	0.3	0.4	1	105	73	93	69	75
10^{-1}	120	0.3	0.4	100	105	73	92	68	75

Z	M_i	α_{ov}	$\Omega/\Omega_{\text{crit}}$	α_{sc}	M_{TAMS}	M_{He}	M_f	M_{CO}	M_{He}
10^{-1}	120	0.5	0.2	1	102	74	95	72	77
10^{-1}	120	0.5	0.2	100	102	74	95	72	77
10^{-1}	120	0.5	0.4	1	104	83	90	80	85
10^{-1}	120	0.5	0.4	100	104	83	90	80	85
SMC	120	0.1	0.2	1	103	54	97	50	56
SMC	120	0.1	0.2	100	103	55	97	50	55
SMC	120	0.1	0.4	1	98	59	89	57	63
SMC	120	0.1	0.4	100	98	60	88	56	63
SMC	120	0.3	0.2	1	91	64	78	63	68
SMC	120	0.3	0.2	100	91	64	78	63	68
SMC	120	0.3	0.4	1	97	68	83	66	72
SMC	120	0.3	0.4	100	97	68	83	65	71
SMC	120	0.5	0.2	1	91	73	80	70	76
SMC	120	0.5	0.2	100	91	73	80	71	76
SMC	120	0.5	0.4	1	92	78	86	76	81
SMC	120	0.5	0.4	100	92	78	86	76	81
10^{-3}	150	0.1	0.2	1	149	79	148	70	79
10^{-3}	150	0.1	0.2	100	149	84	148	77	85
10^{-3}	150	0.1	0.4	1	-	-	149	-	130
10^{-3}	150	0.1	0.4	100	-	-	149	-	129
10^{-3}	150	0.3	0.2	1	149	86	149	64	64
10^{-3}	150	0.3	0.2	100	149	84	149	72	80
10^{-3}	150	0.3	0.4	1	-	-	149	-	129
10^{-3}	150	0.3	0.4	100	-	-	149	-	130
10^{-3}	150	0.5	0.2	1	149	97	148	92	98
10^{-3}	150	0.5	0.2	100	149	97	148	92	98
10^{-3}	150	0.5	0.4	1	-	-	149	-	140
10^{-3}	150	0.5	0.4	100	-	-	149	-	140
10^{-2}	150	0.1	0.2	1	146	79	145	71	79
10^{-2}	150	0.1	0.2	100	146	80	145	72	80
10^{-2}	150	0.1	0.4	1	147	123	147	-	123
10^{-2}	150	0.1	0.4	100	147	129	147	-	129
10^{-2}	150	0.3	0.2	1	146	84	145	69	69
10^{-2}	150	0.3	0.2	100	146	83	142	100	107
10^{-2}	150	0.3	0.4	1	147	131	147	-	131
10^{-2}	150	0.3	0.4	100	147	121	147	-	122
10^{-2}	150	0.5	0.2	1	145	96	144	91	98
10^{-2}	150	0.5	0.2	100	146	96	144	91	98
10^{-2}	150	0.5	0.4	1	-	-	147	-	134
10^{-2}	150	0.5	0.4	100	147	134	147	-	134
10^{-1}	150	0.1	0.2	1	134	73	129	67	74
10^{-1}	150	0.1	0.2	100	134	75	129	68	75
10^{-1}	150	0.1	0.4	1	131	84	119	79	87
10^{-1}	150	0.1	0.4	100	131	84	116	78	86
10^{-1}	150	0.3	0.2	1	129	85	123	82	88
10^{-1}	150	0.3	0.2	100	129	85	123	82	88
10^{-1}	150	0.3	0.4	1	130	91	114	85	92
10^{-1}	150	0.3	0.4	100	130	91	114	84	93
10^{-1}	150	0.5	0.2	1	118	95	104	92	98
10^{-1}	150	0.5	0.2	100	118	95	103	92	98
10^{-1}	150	0.5	0.4	1	128	104	112	100	107
10^{-1}	150	0.5	0.4	100	128	104	112	100	106

Z	M_i	α_{ov}	$\Omega/\Omega_{\text{crit}}$	α_{sc}	M_{TAMS}	M_{He}	M_{f}	M_{CO}	M_{He}
SMC	150	0.1	0.2	1	124	71	116	67	74
SMC	150	0.1	0.2	100	122	72	113	66	73
SMC	150	0.1	0.4	1	120	77	105	74	81
SMC	150	0.1	0.4	100	120	77	99	72	80
SMC	150	0.3	0.2	1	110	82	91	81	87
SMC	150	0.3	0.2	100	110	82	93	81	87
SMC	150	0.3	0.4	1	120	88	97	86	92
SMC	150	0.3	0.4	100	119	88	100	85	92
SMC	150	0.5	0.2	1	115	93	101	90	97
SMC	150	0.5	0.2	100	115	94	101	90	97
SMC	150	0.5	0.4	1	112	98	107	95	101
SMC	150	0.5	0.4	100	112	98	107	95	101

APPENDIX B: RESOLUTION TEST

In order to ensure that our chosen resolution was converged, we conducted a resolution test which we define here. As of version r15140, MESA has two forms of top-level resolution definition for controlling temporal and spatial resolutions - these are *time_delta_coefficient* and *mesh_delta_coefficient*, though there are many more parameters which exist (for examples and included resolution tests, there is Farmer et al. (2019) and Costa et al. (2022)). This version is the first to include the *time_delta_coefficient* parameter. Previously, resolution control for the time domain was achieved through varying *varcontrol_target*. This is now discouraged, and a limit of *varcontrol_target* $> 1d - 4$ is imposed by default, though this can be overridden. For completeness, variations in *varcontrol_target* were also tested.

To attempt to optimise the resolution which would eventually be chosen, the evolution of the star up to the end of core Helium burning was split into two stages. In this way, the resolution could be tailored to each burning stage to provide converged results as quickly as possible. The first stage covered the star’s evolution from Hydrogen ignition at the Zero Age Main Sequence (ZAMS) to the Terminal Age Main Sequence (TAMS). Picking up where the first stage left off, the second stage continues the life of the star to the end of Helium burning in the core.

When splitting the model, we took advantage of a feature present in MESA which allows a model to be saved upon termination of the run. However, this does not save the internal profile of the model upon termination, unlike the *photo* files. MESA warns that this is the case, and further suggests that this shouldn’t cause particularly egregious divergences between a model run from the *.mod* file or run as one continuous model. However, for our test case, it was found that considerable differences could be seen in the later stages of evolution for stars run in our grid. For the purposes of the resolution test, since the tests were to examine convergence, using the *.mod* files was acceptable as the physics does not change, merely the internal structure.

Three series of tests were conducted. One which varied *time_delta_coefficient*, another varying *varcontrol_target* and a final smaller series varying *mesh_delta_coefficient*. During the Main Sequence stage, all resolutions showed consistent results for the final properties of the model, which can be seen in the left-hand panels of Figures B1, B2, and B3. While *varcontrol_target* shows a convergence towards $1d - 4$, it is noted that the range of values which this encompasses are small in comparison to the total model. The spatial resolution test, *mesh_delta_coefficient*, showed little variation between models as well at this stage, as did *time_delta_coefficient*.

When moving into the core Helium burning stage, *time_delta_coeff* showed a bifurcation in the results, showcased in the right-hand panel of Figure B2. While most models would act typically, and complete core Helium burning in an expected manner (herein referred to as “Case 1”), some models would appear to continue past Helium burning. For the models which kept going (herein described as “Case 2”), the error started near the end of where Helium burning should’ve ended, at which point a small error regarding minimum abundances propagated. These errors compounded, which eventually leads to the model continuing past core Helium burning into core Carbon burning. If running the MESA “Vink” wind recipe, the model will lose as much as $30 M_{\odot}$. However, if using the corrected iron abundance recipe mentioned before, the star will still lose mass, but only $2 \sim 3 M_{\odot}$ in comparison. This is due to how each recipe handles the metallicity dependence of Vink et al. (2001). In default MESA “Vink” wind, this recipe accounts for all metals present at the surface of the star when calculating the mass loss in each timestep.

This however, is incorrect, and instead the recipe should only depend on surface iron abundances.

Upon deeper investigation, this issue was caused by use of the “exponential” overshooting prescription in MESA. Thus, by using the “step” overshooting prescription in MESA, the models would not encounter the same issues with regards to abundance changes, and the follow-on errors which occurred. Exponential overshooting will produce a gradient of elements and products of the CNO cycle above the core as this is mixed in gradually. If the shell dips downwards in to the core during the early core Helium burning stage, then this would cause a change of one of the CNO elements in the Hydrogen-burning shell region’s boundary. As the shell region is fully convective, and full convection results in instantaneous mixing. This leads to an over-abundance of a CNO element throughout the shell. MESA would then correct for this by increasing the abundances of the other elements - over-correcting the abundance. When this occurs, the model evolves as per the Case 2 model, rather than the typical Case 1 model. Some time after, the entire star becomes convective, which mixes the high abundance of metals all the way to the surface, where the wind is calculated, which thus produces the unrealistically high mass-loss rates.

Whereas exponential overshooting, by its name, exponentially reduces the overshooting over a distance parameter f_0 , step overshooting is instead a simple function of extending the core by a distance described by α_{ov} . This means that all elements in this region are fully mixed, and so when the shell touches the step overshooting region as it does in the Case 2 models mentioned before, there is no gradient of elements that the shell then corrects for. This is then fully mixed, which avoids the correction.

Given the results of our resolution test, we decide to use a value of *varcontrol_target* of $2d - 4$, while both *time_delta_coefficient* and *mesh_delta_coefficient* were left at their default values. Additionally, we use the step overshooting prescription.

APPENDIX C: HIGH Ω MODELS, AND Ω AT LOW Z

In Section 4, we have discussed the effects we have observed in our models, including the effects of low versus high rotation. Another effect which we have also discussed is the spin-up to supercritical breakup speeds for rotation as a function of decreasing metallicity, the conclusion of which is illustrated by Figure 7. With this appendix, we will summarise our results in the context of current and potential future work.

As mentioned, we find a metallicity-dependent limit of rotation which could prohibit formation of heavy black holes at lower metallicity. We also expect the distribution of rotation rates to shift upwards at lower metallicity due to the lack of angular momentum loss through winds, which would further truncate the limit on the number of black holes with $M_{BH} > 50 M_{\odot}$.

There is evidence from earlier works such as Meynet et al. (2006) which show that a star which reaches breakup velocity and become unbound experiences a period of intense mass loss until the remaining star can become gravitationally bound again. For models in Meynet et al. (2006), this was achieved by removing supercritical layers, then allowing the star to stabilise, which resulted in mass loss in the range of $35 \sim 42 M_{\odot}$ from a $60 M_{\odot}$ star at varying metallicity and rotation rates (see Table 1 from aforementioned paper). We can estimate from this that the mass loss for our stars, which are the same mass or greater than those of Meynet et al. (2006) would be similarly dramatic.

In a small subset of models, we implemented the $\Gamma\Omega$ mass loss boost factor of Maeder & Meynet (2000b) which we find can dramati-

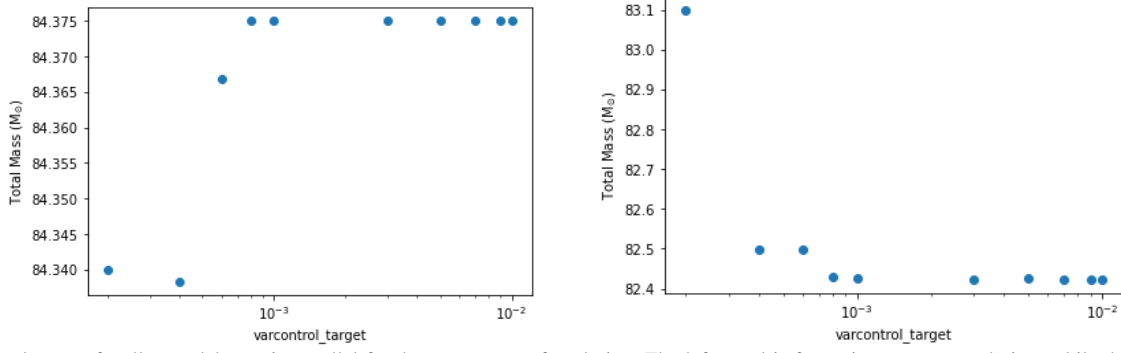


Figure B1. Final mass of stellar models run in parallel for the same stage of evolution. The left panel is for main sequence evolution, while the right panel is for TAMS until core-Helium exhaustion. All models were started from the same initial model, except for a different resolution parameter - in this case, *varcontrol_target*.

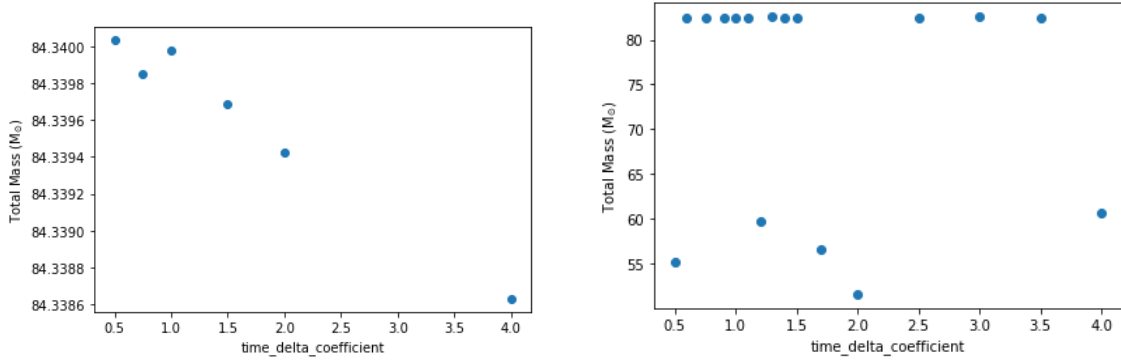


Figure B2. Similar to the above panel, except that instead of *varcontrol_target*, the varying resolution parameter is *time_delta_coeff*. The bifurcation of results can be seen in the right panel, covering TAMS to core-Helium exhaustion. Where some results would remain above $80 M_{\odot}$, others would lose as much as $30 M_{\odot}$ of stellar material.

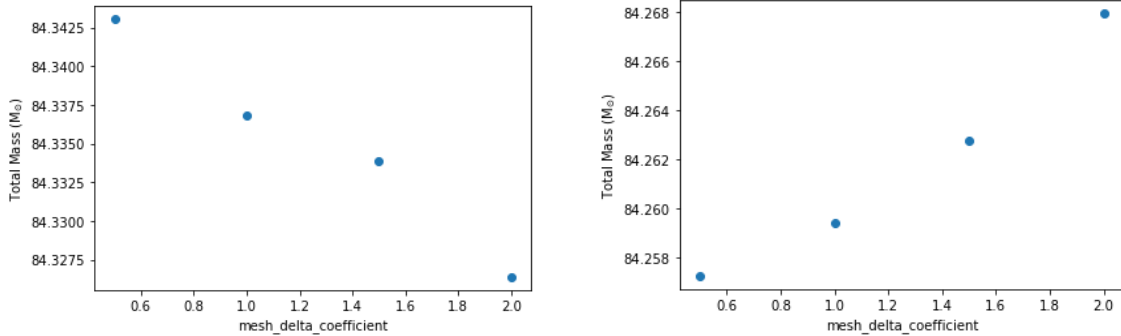


Figure B3. Initial tests conducted with varying *mesh_delta_coeff* for each stage. Hydrogen burning is shown on the left, while Helium burning is on the right as before.

cally change the effect of rotation in the high rotation, low metallicity regime. Firstly, the effect of this boost allows the model to avoid becoming supercritical by boosting the mass loss as a factor given in Equation C1, which increases dramatically as the rotation rate gets close to critical, thus allowing more angular momentum to be lost before the model becomes supercritical. This was seen to stop models from reaching breakup speeds up to initial rotation values of $\Omega/\Omega_{\text{crit}} = 0.8$.

The MESA implementation of rotation boosted mass loss is from Heger et al. (2000) and Langer (1998), where mass loss is boosted by a parameter of $[1/(1 - \Omega/\Omega_{\text{crit}})]^{\xi}$, where ξ is the fit value, nominally $\xi = 0.43$. This, however, does not account for the von

Zeipel theorem (Maeder & Meynet 2000b). In Maeder & Meynet (2000b), the equation of rotation boosted mass loss is as follows;

$$\frac{\dot{M}(\Omega)}{\dot{M}(0)} \simeq \frac{(1 - \Gamma)^{\frac{1}{\alpha} - 1}}{\left[1 - \frac{\Omega^2}{2\pi G \rho_m} - \Gamma\right]^{\frac{1}{\alpha} - 1}} \quad (\text{C1})$$

which is given in their equation 4.29 and correctly accounts for the von Zeipel theorem.

Rotation in MESA is handled as a diffusive mixing process (Paxton et al. (2013), Section 6.1.2 for MESA implementation, and references therein for complete physical descriptions) compared to other stellar evolution codes which handle rotation as diffusion-advection approach, notably the GENEC stellar evolution code (Eggenberger

et al. 2008). The main difference between these two methods arises in the transport of angular momentum, as the diffusive process determined used by MESA considers various instabilities, discussed briefly in Section 2 of this paper, and in more detail in Heger et al. (2000), while GENEC uses the formulae of Maeder & Zahn (1998).

Overall, we cannot say exactly where the maximum $\Omega/\Omega_{\text{crit}}$ limit is in the context of wider physical processes - in our grid, this appears at $\Omega/\Omega_{\text{crit}} = 0.4$ and decreases with metallicity. Results from previous work suggests this limiting value could be higher, while a different stellar evolution code could suggest a different number. Thus, at this time, we have provided a fiducial investigation which informs future work.

APPENDIX D: ENHANCED WINDS IN CLOSE PROXIMITY TO THE EDDINGTON LIMIT

As discussed in Sect. 2, the mass-loss recipe employed in this study is identical to the one in Vink et al. (2021). Since that work, we have implemented mass-loss rate relations for very massive stars in close proximity to the Eddington limit from Vink et al. (2011) for both high and low Z (Sabhanit et al. 2022, 2023).

Figure D1 indicates the parameter space of these very massive star models for which a new mass-loss recipe was implemented, in comparison to the parameter space of the current study. The figure shows the optical thickness of winds as a function of metallicity and initial mass. The evolutionary models from Vink et al. (2021) that produce the highest final masses and BH masses are highlighted by the yellow box. These winds remain optically thin and a mass-loss boost would not be applied.

The entire parameter space of the current models is encapsulated by the yellow dashed line, where the winds are either totally or partially optically thin (as shown in the orange background). These models are on the verge of becoming optically thick. Comparison of the models in our current study compared to those of (Sabhanit et al. 2022, 2023) shows that our results are not affected by a mass-loss boost.

In short, the reason why the mass-loss recipe applied in the current study and the ones in Sabhanit et al. (2022, 2023) are equivalent is that the parameter space of our current study is almost entirely in the optically thin regime of Sabhanit et al. (2022, 2023).

APPENDIX E: INFLATION AND MLT++ AT LOW METALLICITY

MLT++ is known to affect the inflation characteristics of MESA models, however it is also necessary to allow massive star models to evolve without convergence issues (as discussed in Section 2.1). We ran a $M_{\text{ZAMS}} = 93 M_{\odot}$ model with low overshooting (~ 0) and without MLT++ in order to test if the maximum BH mass we predict is robust. The reason this is an appropriate test is that at very low metallicity you would not expect to witness a large envelope inflation. However, at a higher metallicity ($1/50 Z_{\odot}$), massive stars with M_{ZAMS} above $80 M_{\odot}$ may evolve into supergiants during core Hydrogen burning (Szécsi et al. 2015). We apply a very low metallicity ($Z = 1/1000$ th Z_{\odot}) from our prediction in Section 5. With these conditions, the model is able to remain compact for the He burning lifetime and not undergo inflation, which will not necessarily be true for the rest of the parameter space. While the envelope mixing choice may, similarly to mass-loss assumptions as discussed in Vink et al. (2021), affect the cut-off point on the maximum BH mass with Z ,

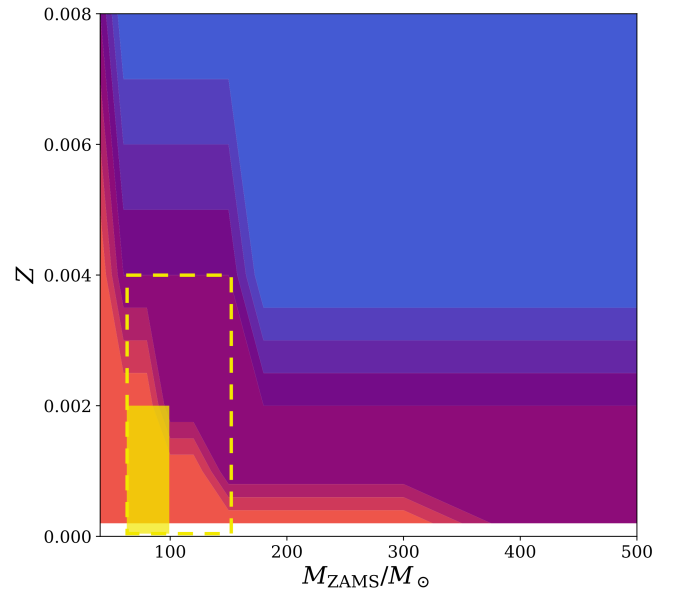


Figure D1. Sketch of optical wind thickness as a factor of metallicity and ZAMS mass. The blue region denotes the region where the star has a high Γ_e for the entire main sequence, while the orange region describes a star has a low Γ_e for the entire main sequence. Purple has a high Γ_e on the cool side of the bi-stability jump (Sabhanit et al. 2023). Our grid is bounded by the yellow dashed line, while the models with highest final masses ($M_{\text{final}} > 50 M_{\odot}$) and $M_{\text{CO}} < 36.3 M_{\odot}$ are denoted by the yellow box.

the sheer maximum BH mass value that is expected to be achieved at the lowest Z values, is not expected to depend on our decision to use MLT++.

This paper has been typeset from a $\text{\TeX}/\text{\LaTeX}$ file prepared by the author.